

AD-A125 703

A COMPARISON OF SEVERAL SYSTEMS FOR TRANSMISSION
MEASUREMENTS AT 94 GHZ..(U) OHIO STATE UNIV COLUMBUS
ELECTROSCIENCE LAB . O M BUYUKDURA ET AL. FEB 82
ESL-713671-1 AFWAL-TR-81-1281

1/1

UNCLASSIFIED

F/G 14/2

NL

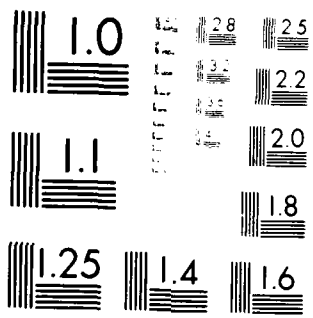
END

DATE

FILED

1 83

DTIC



U.S. GOVERNMENT PRINTING OFFICE: 1963

AFWAL-TR-81-1281

A COMPARISON OF SEVERAL SYSTEMS FOR TRANSMISSION
MEASUREMENTS AT 94 GHZ

O. M. BUYUKDURA, C. A. LEVIS

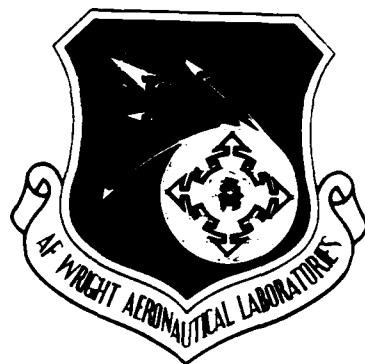
OHIO STATE UNIVERSITY ELECTROSCIENCE LABORATORY
COLUMBUS, OHIO 43212

FEBRUARY 1982

INTERIM REPORT FOR PERIOD APRIL 1981 - AUGUST 1981

APPROVED FOR PUBLIC RELEASE; DISTRIBUTION UNLIMITED

AVIONICS LABORATORY
AIR FORCE WRIGHT AERONAUTICAL LABORATORIES
AIR FORCE SYSTEMS COMMAND
WRIGHT-PATTERSON AIR FORCE BASE, OHIO 45433



AD A 1 237 03

DTIC FILE COPY

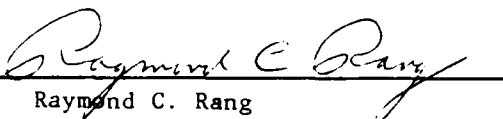


NOTICE

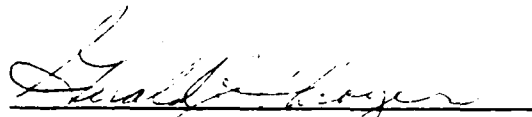
When Government drawings, specifications, or other data are used for any purpose other than in connection with a definitely related Government procurement operation, the United States Government thereby incurs no responsibility nor any obligation whatsoever; and the fact that the government may have formulated, furnished, or in any way supplied the said drawings, specifications, or other data, is not to be regarded by implication or otherwise as in any manner licensing the holder or any other person or corporation, or conveying any rights or permission to manufacture use, or sell any patented invention that may in any way be related thereto.

This report has been reviewed by the Office of Public Affairs (ASD/PA) and is releasable to the National Technical Information Service (NTIS). At NTIS, it will be available to the general public, including foreign nations.

This technical report has been reviewed and is approved for publication.

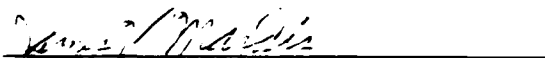


Raymond C. Rang
Project Engineer
EO Systems Group
Avionics Laboratory



Gerald J. Shroyer, Chief
EO Systems Group
Mission Avionics Division
Avionics Laboratory

FOR THE COMMANDER



James V. Mardis, Lt Col, USAF
Electro-Optics Branch
Mission Avionics Division
Avionics Laboratory

"If your address has changed, if you wish to be removed from our mailing list, or if the addressee is no longer employed by your organization please notify AFWAL/AARI-1, W-PAFB, OH 45433 to help us maintain a current mailing list".

Copies of this report should not be returned unless return is required by security considerations, contractual obligations, or notice on a specific document.

UNCLASSIFIED

SECURITY CLASSIFICATION OF THIS PAGE (When Data Entered)

REPORT DOCUMENTATION PAGE		READ INSTRUCTIONS BEFORE COMPLETING FORM
1. REPORT NUMBER AFWAL-TR-81-1281	2. GOVT ACCESSION NO. AD-A125703	3. RECIPIENT'S CATALOG NUMBER
4. TITLE (and Subtitle) A COMPARISON OF SEVERAL SYSTEMS FOR TRANSMISSION MEASUREMENTS AT 94 GHZ		5. TYPE OF REPORT & PERIOD COVERED Interim Report for Period April 1981 - August 1981
		6. PERFORMING ORG. REPORT NUMBER ESL-713671-1 ✓
7. AUTHOR(s) O.M. Buyukdura and C.A. Levis		8. CONTRACT OR GRANT NUMBER(s) F33615-81-C-1437
9. PERFORMING ORGANIZATION NAME AND ADDRESS Ohio State University ElectroScience Laboratory Columbus, Ohio 43212		10. PROGRAM ELEMENT PROJECT, TASK AREA & WORK UNIT NUMBERS 2004 05 57
11. CONTROLLING OFFICE NAME AND ADDRESS Avionics Laboratory (AFWAL/AARI) AF Wright Aeronautical Laboratories, AFSC Wright-Patterson Air Force Base, Ohio 45433		12. REPORT DATE February 1982
14. MONITORING AGENCY NAME & ADDRESS (if different from Controlling Office)		13. NUMBER OF PAGES 96
		15. SECURITY CLASS. (of this report) Unclassified
15a. DECLASSIFICATION DOWNGRADING SCHEDULE		
16. DISTRIBUTION STATEMENT (of this Report) Approved for public release; distribution unlimited.		
17. DISTRIBUTION STATEMENT (of the abstract entered in Block 20, if different from Report)		
18. SUPPLEMENTARY NOTES		
19. KEY WORDS (Continue on reverse side if necessary and identify by block number) Propagation Radar Transmissometer Millimeter wave Transmittance Rain		
20. ABSTRACT (Continue on reverse side if necessary and identify by block number) Five systems for transmission measurements at 94 GHz were compared. The systems are: two-ended with square-law detector, single-ended with square-law detector, single-ended with chopped signal transmission and quadrature receiver, single-ended with pulsed source and incoherent integration, and single-ended with pulsed source and quadrature receiver. The signal-to-noise ratio expressions for the output of each receiver are given. The signal-to-noise ratios are presented as functions of range,		

DD FORM 1473

JAN 73

EDITION OF 1 NOV 65 IS OBSOLETE

UNCLASSIFIED

SECURITY CLASSIFICATION OF THIS PAGE (When Data Entered)

UNCLASSIFIED

SECURITY CLASSIFICATION OF THIS PAGE(When Data Entered)

(continued)

and the ranges corresponding to $(S/N)=10$ are plotted versus specific attenuation. The computer programs that generate these curves for each system are also given. Expressions and computer subroutines to calculate the attenuation due to rain are included.

The two-ended system gives the best performance. Of the single-ended systems, which are more convenient to use, the one with a quadrature receiver gives the best results.

UNCLASSIFIED

SECURITY CLASSIFICATION OF THIS PAGE(When Data Entered)

FOREWORD

This report was presented as a thesis in partial fulfillment of the degree Master of Science at The Ohio State University.

The work reported here was supported in part by the Air Force Systems Command, Rome Air Development Center, Griffiss Air Force Base, New York 13441 under Contract F30602-78-C-0102, which preceded the current contract.



A

TABLE OF CONTENTS

	Page
FOREWORD	iii
SECTION	
I INTRODUCTION	1
II THE SYSTEM PERFORMANCE EQUATIONS	3
A. Derivation of Pre-Detection Signal-to-Noise Ratio Expressions	3
B. Processed Signal-to-Noise Ratio Expressions	6
1. One-way transmission and square-law detection	6
2. Two-way transmission and square-law detection	8
3. Chopped signal transmission and quadrature receiver	9
4. Pulsed source and incoherent pulse integration	16
5. Pulsed source and quadrature receiver	17
C. Attenuation Due to Rain and Fog	20
D. Summary	21
III RESULTS.	22
A. System Calculations	22
B. Results and Discussions	24
C. Rain Attenuation	43
D. Conclusions	46
APPENDIX A - SCATTERING FROM A SPHERE	50
APPENDIX B - GENERATION OF THE SPHERICAL WAVE FUNCTIONS . .	60
Reference -	64

SECTION I

INTRODUCTION

The aim of this study has been to compare the expected performance of several instrumentation systems for measuring transmission at 94 GHz under various weather conditions. This frequency was selected because it is one of the "windows" of low molecular absorption as shown in Figure 1. The problem of calculating the attenuation through rain and fog due to scattering and absorption in terms of meteorologically measurable quantities was also attacked as a part of the system evaluation problem.

The following receiver systems were studied:

1. Square-Law Detection,
2. Quadrature Receiver,
3. Post-Detection Integration.

The receiver with a square-law detector was considered both in a one-way transmission system and in a two-way transmission system with the use of a calibrated target, i.e., as a radar transmissometer. In both cases, the receiver signal was considered to be chopped at an audio frequency. The quadrature receiver was studied for the reception of both continuous-wave and pulsed signals in the radar transmissometer configuration. The receiver which employs post-detection integration was considered to be used with a pulsed transmitter: a standard pulse radar configuration.

The signal-to-noise ratio expressions and an expression for attenuation by rain and fog are given in Section II. The results obtained from computer programs utilizing these equations are contained in Section III.

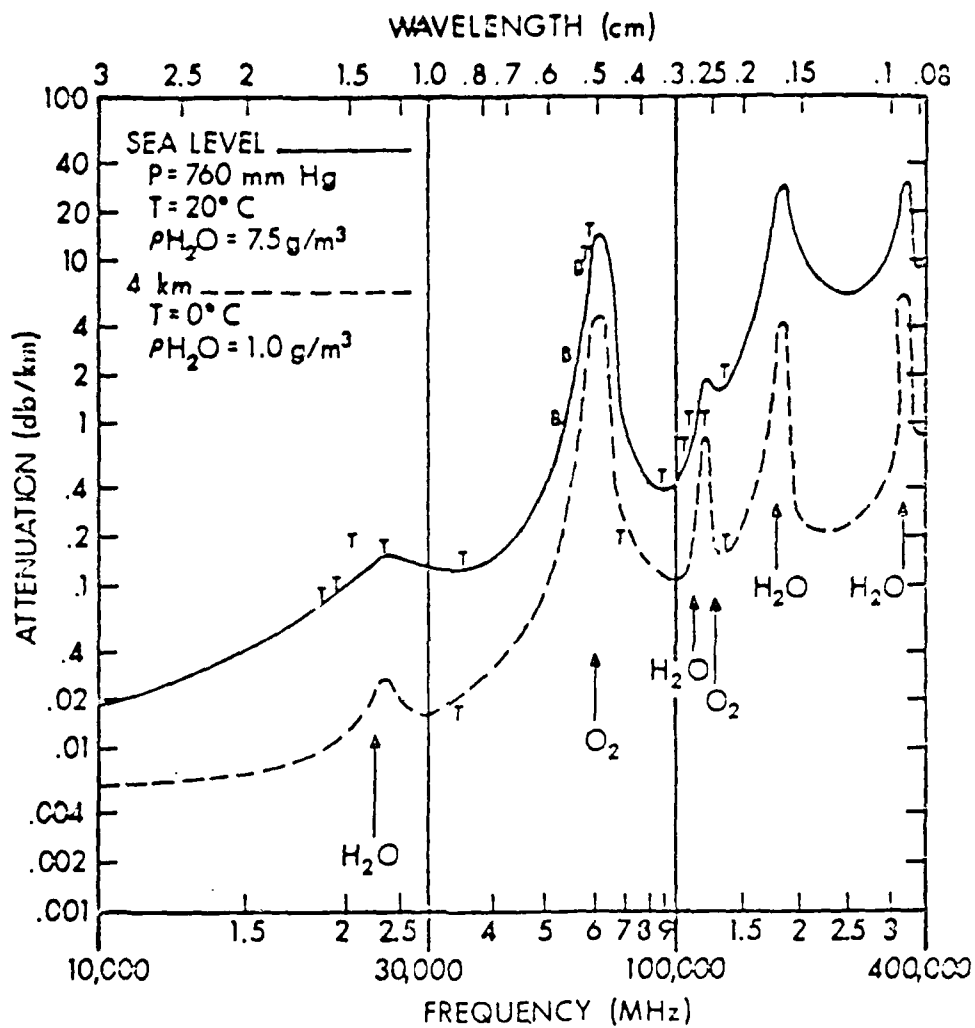


Figure 1. Specific attenuation in clear air versus frequency (after Rosenblum [1]).

SECTION II

THE SYSTEM PERFORMANCE EQUATIONS

The range at which an output signal-to-noise ratio of 10 dB would be realized was taken as a criterion of system performance. Therefore, the aim of this section is to derive signal-to-noise ratio expressions for the five types of instrumentation which were presented in Section I. As a first step, the signal-to-noise ratio expressions for the receiver systems will be derived at a point before any detection or non-linear signal processing is employed, i.e., at the output of the intermediate frequency amplifier. These expressions depend on whether a one-way path or a two-way (radar) mode is considered, but they do not depend on the type of signal detection employed.

A. Derivation of Pre-Detection Signal-to-Noise Ratio Expressions

Each system falls into one of the following two groups:

1. The system utilizes the transmission of a signal over a one-way path, or
2. the receiver is located physically close to the transmitter and the signal from the transmitter is reflected from a calibrated target to the receiver. In essence, this is a radar system although without a requirement for range resolution.

For systems of the first kind, the power density at the receiver antenna is given by

$$p = \frac{P_t G_t}{4\pi R^2} \quad , \quad (1)$$

where P_t is the transmitted power, G_t is the transmitter antenna gain in the direction of the receiver, and R is the distance between the transmitter and receiver antennas, all in consistent units. Then, the received power is given by

$$P_r = \frac{P_t G_t}{4\pi R^2} A_e \quad , \quad (2)$$

where P_r is the power received by the receiving antenna and A_e , in units of area, is the effective aperture of the receiving antenna, given by

$$A_e = \frac{G_r \lambda^2}{4\pi} \quad , \quad (3)$$

where G_r is the gain of the receiver antenna in the direction of the transmitter, and λ is the wavelength of the signal. Thus, from Equations (2) and (3), one obtains the transmission equation given by [2]

$$P_r = \frac{P_t G_t G_r \lambda^2}{(4\pi)^2 R^2} \quad . \quad (4)$$

If there are attenuating factors over the path of propagation such as rain or fog, and if there is loss in the transmitter and receiver systems, then the inclusion of these effects leads to

$$P_r = \frac{P_t G_t G_r \lambda^2 L_t L_r}{(4\pi)^2 R^2} 10^{-\alpha R/10} \quad , \quad (5)$$

where α is the specific attenuation in decibels per unit length, and L_t and L_r are transmitter-to-antenna and antenna-to-receiver component losses, respectively.

The thermal noise power at the output of the pre-detection filter (usually simply the intermediate frequency amplifier) is

$$N = kT_0 BF \quad , \quad (6)$$

where k is Boltzmann's constant (1.38×10^{-23} joules/K), B is the effective receiver pre-detection filter bandwidth (Hertz), T_0 is the reference noise temperature (290 K), and F is the noise figure of the receiver referred to 290 K.

Thus, from Equations (5) and (6), one obtains

$$(S/N) = \frac{P_t G_t G_r^2 L_t L_r}{(4\pi)^2 R^2 k T_0 B F} 10^{-\alpha R/10} \quad . \quad (7)$$

This is the signal-to-noise ratio at the output of the intermediate-frequency amplifier for one-way transmission.

For systems of the radar type, the power density at the target is given by

$$p_t = \frac{P_t G_t L_t}{4\pi R^2} 10^{-\alpha R/10} \quad . \quad (8)$$

The power reradiated in the receiver direction is

$$p' = \frac{P_t G_t L_t \sigma}{4\pi R^2} 10^{-\alpha R/10} \quad , \quad (9)$$

where σ , in units of area, is the radar cross section of the target. The power density of the echo signal at the receiver antenna is given by

$$p = \frac{P_t G_t L_t \sigma}{(4\pi R^2)^2} 10^{-2\alpha R/10} \quad , \quad (10)$$

and the received power is obtained by multiplying p by the effective area of the aperture, leading, by use of Equation (3), to the radar equation including losses [2],

$$P_r = \frac{P_t G_t G_r^2 L_t L_r}{(4\pi)^3 R^4} 10^{-2 R/10} \quad (11)$$

Thus, using Equations (6) and (11), the pre-detection signal-to-noise ratio for the radar transmissometer is

$$(S/N) = \frac{P_t G_t G_r^2 L_t L_r}{(4\pi)^3 R^4 k T_o B F} 10^{-2 R/10} \quad (12)$$

Equations (7) and (12) give the pre-detection signal-to-noise ratio expressions for the two transmitter-receiver geometries.

B. Processed Signal-to-Noise Ratio Expressions

In this section, the five systems introduced in Section I will be discussed, and for each one the expression for signal-to-noise ratio, after detection and signal processing has been employed, will be given.

1. One-way transmission and square-law detection

This system transmits and receives a chopped signal over a one-way path. At the receiver, the signal is heterodyned to an intermediate frequency, amplified, and detected by a square-law device which is followed by a narrow-band (audio) filter as shown in the block diagram in Figure 2. The signal-to-noise ratio expression in Equation (7) applies to $r(t)$.

The chopped signal will be approximated by an amplitude-modulated signal with a modulation index of 100% since only the fundamental harmonic term of the signal will be picked up by the audio filter, so that the input to the square-law device is

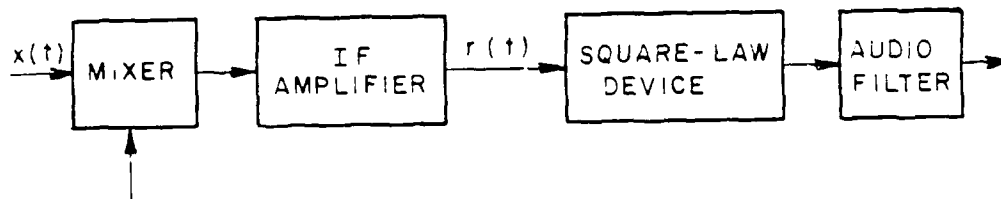


Figure 2. Receiver system with square-law detector.

$$r(t) = A_c [1 + \mu \cos \omega_a t] \cos \omega_c t + n(t) \quad (13)$$

where A_c is the carrier amplitude, μ is the modulation index, $n(t)$ is narrowband Gaussian noise with spectral density determined by the spectral response of the intermediate-frequency amplifier and centered at the intermediate angular frequency ω_c , and ω_a is the angular center frequency of the audio filter which is equal to the angular frequency of the chopped signal. Typical values for $\omega_a/2\pi$ and $\omega_c/2\pi$ are 1 kHz and 1 GHz, respectively.

The signal-to-noise power ratio at the output of the audio filter for such a system and the input as given in Equation (13) is given by [3]

$$(E/N) = \mu^2 (S/N)^2 \left\{ \frac{B_{if}}{B_a} [1 + (S/N)(2 + \mu^2)] \right\}^{-1} \quad (14)$$

where (S/N) is the pre-detection signal-to-noise ratio, B_{if} is the equivalent rectangular bandwidth of the intermediate-frequency amplifier, and B_a is the bandwidth of the audio filter. Finally, for a modulation index of 100%, Equation (14) becomes

$$(E/N) = \frac{(S/N)^2 \left(\frac{B_{if}}{B_a} \right)}{1 + 3(S/N)} \quad (15)$$

with (S/N) as given in Equation (7).

This is the required expression for systems employing a chopped-waveform signal and square-law detection.

2. Two-way transmission and square-law detection

In this system, the receiver is identical to that of the previous system. This time, however, a target is used and the reflected signal

from this target is received. Thus, the processed signal-to-noise ratio is again given by Equation (15), but with (S/N) as given by Equation (12).

3. Chopped signal transmission and quadrature receiver

This system also consists of the transmission of a chopped signal over a two-way path with the use of a target. In contrast to the system discussed previously, a quadrature detector is used in the receiver as shown in the block diagram of Figure 3, where $u(t)$ is the unit step function, which is introduced here only to show that the integrators are reset at $t=0$, so that earlier signals are disregarded. If the integrators, which are discontinuously operating devices, are replaced with equivalent continuously operating filters as discussed below, then the $u(t)$ should be omitted, thus the signals at the input to the detector are identical for Figures 2 and 3. For mathematical convenience, the integrators will be used in deriving the output signal-to-noise ratio.

Following Schwartz[4], to obtain the output signal-to-noise ratio, first a single correlation detector will be considered as shown in Figure 4a. The output of the integrator is given by

$$y(T) = \int_0^T r(t)s(t)dt \quad . \quad (16)$$

Now, consider the matched filter arrangement of Figure 4b. The output of the filter at $t=T$ is given by

$$y(T) = \int_{-\infty}^{\infty} r(t)u(t)h(T-t)dt \quad . \quad (17)$$

By the definition of the unit step function, and the causality requirement for the filter, we have

$$u(t) \equiv 0 \quad \text{for } t < 0 \quad , \quad (18)$$

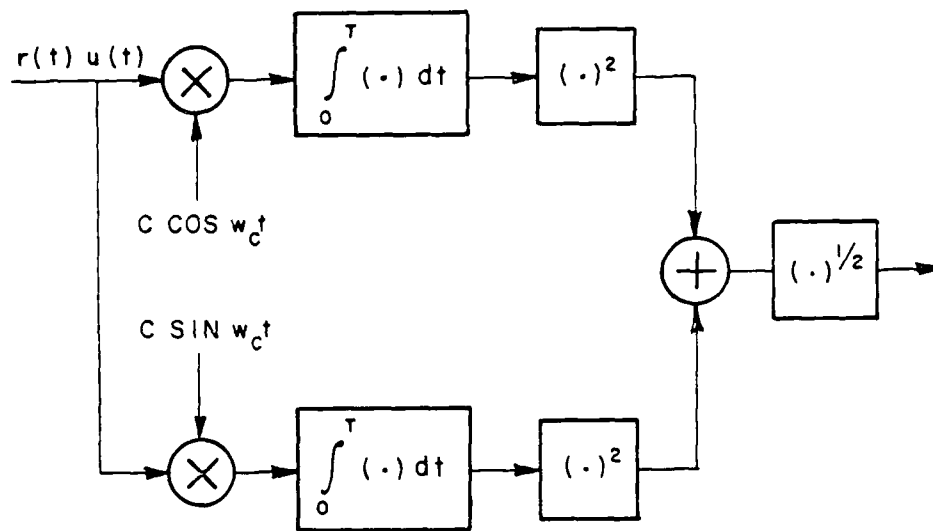
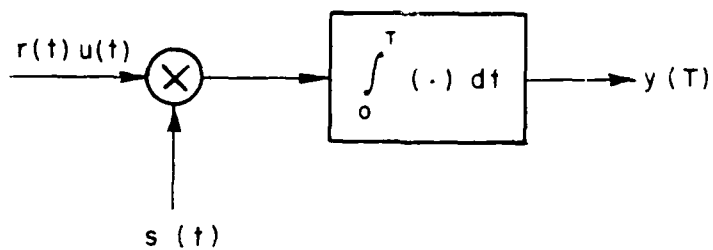
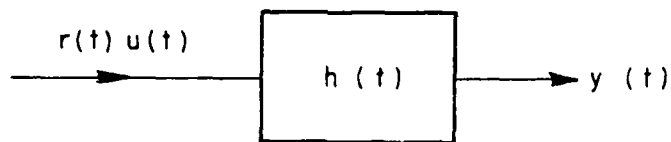


Figure 3. Quadrature receiver.



(a)



(b)

Figure 4. a) Correlation detector
b) Matched filter.

and

$$h(T-t) \equiv 0 \text{ for } t > T \quad . \quad (19)$$

Combining Equations (18) and (19) with Equation (17), one obtains

$$y(T) = \int_0^T r(t)h(T-t)dt \quad . \quad (20)$$

If the filter impulse response satisfies

$$h(T-t) = s(t) \text{ for } 0 < t < T \quad , \quad (21a)$$

or equivalently,

$$h(t) = s(T-t) \text{ for } t > 0 \quad , \quad (21b)$$

then $y(T)$ is the same as in the correlation detector. Explicitly, the signals in Figure 4a are,

$$r(t) = A \cos \omega_c t \quad , \quad (22)$$

$$s(t) = C \cos \omega_c t \quad , \quad (23)$$

and, from Equation (20), the filter impulse response which makes it equivalent to the integrator must be

$$h(t) = C \cos \omega_c (T-t) \quad . \quad (24)$$

If T is chosen to be an integer multiple of the period of $r(t)$, i.e.,

$$T = \frac{2\pi n}{\omega_c} \quad (25)$$

then Equation (24) becomes

$$h(t) = C \cos[2\pi n - \omega_c t] = C \cos \omega_c t = s(t) \quad , \quad (26)$$

and imposing the conditions in Equations (18) and (19), one obtains

$$h(t) = C \cos \omega_c t u(t)u(T-t) \quad . \quad (27)$$

The transfer function of the filter given by the Fourier Transform of its impulse response is

$$H(\omega) = C \int_0^T \cos \omega_c t e^{j\omega t} dt \quad . \quad (28)$$

Carrying out the integration, one obtains

$$H(\omega) = \frac{CT}{2} e^{j(\omega+\omega_c)\frac{T}{2}} \frac{\sin \frac{(\omega+\omega_c)\frac{T}{2}}{\frac{\omega+\omega_c}{2}}}{\frac{\omega+\omega_c}{2}} + e^{j(\omega-\omega_c)\frac{T}{2}} \frac{\sin \frac{(\omega-\omega_c)\frac{T}{2}}{\frac{\omega-\omega_c}{2}}}{\frac{\omega-\omega_c}{2}} \quad (29)$$

Since the system shown in Figure 3 is linear, the signal and noise components of the output may be treated separately. The desired signal at the output is obtained directly from Figure 4a and Equations (22) and (23) as

$$y(T) = \int_0^T AC \cos \omega_c t dt = \frac{ACT}{2} \quad , \quad (30)$$

which leads to the expression for the signal power

$$P_s = \left(\frac{ACT}{2} \right)^2 \quad . \quad (31)$$

The noise power is given by [5]

$$P_n = \frac{1}{2\pi} \int_{-\infty}^{\infty} S_{ny}(\omega) d\omega \quad , \quad (32)$$

where $S_{ny}(\omega)$ is the power spectral density of the noise component of $y(t)$ which, in terms of the power spectral density of the noise component of the input is given by

$$S_{ny}(\omega) = S_{nr}(\omega) |H(\omega)|^2 \quad (33)$$

Since, for a filter with a rectangular frequency response, with bandwidth B and with unit amplitude, the noise power at the output is given by

$$P_n = FkT_o B \quad (34)$$

then, assuming a flat input noise power spectral density, from Equations (32) and (34), one obtains

$$S_{nr}(\omega) = \frac{FkT_o}{2} \quad (35)$$

For $H(\omega)$ as given in Equation (29), the noise power at the output is given by

$$P_n = \frac{1}{2\pi} S_{nr} \int_{-\infty}^{\infty} |H(\omega)|^2 d\omega \quad (36)$$

Assuming $\omega_c \gg \frac{2\pi}{T}$, and using Equation (29), Equation (36) becomes

$$P_n = \frac{1}{\pi} S_{nr} \frac{C^2 T^2}{4} \int_0^{\infty} \frac{\sin^2\left(\frac{\omega - \omega_c}{2} T\right)}{\left[\frac{\omega - \omega_c}{2}\right]^2} d\omega \quad (37)$$

Changing the variable of integration, one obtains

$$P_n = \frac{1}{\pi} S_{nr} \frac{C^2 T^2}{4} \cdot \frac{2}{T} \int_{-\frac{\omega_c T}{2}}^{\infty} \left(\frac{\sin x}{x}\right)^2 dx \quad (38)$$

Imposing $\omega_c \gg \frac{2\pi}{T}$ once more, and evaluating the integral yields

$$P_n = \frac{1}{\pi} S_{nr} \frac{C^2 T}{2} \int_{-\infty}^{\infty} \left(\frac{\sin x}{x} \right)^2 dx = \frac{S_{nr} C^2 T}{2} \quad (39)$$

Combining Equations (35) and (39), the noise power is given by

$$P_n = FkT_0 \frac{C^2 T}{4} \quad (40)$$

An input signal with unknown phase may be expressed as

$$r(t) = A \cos(\omega_c t + \theta) \quad (41)$$

where θ is a random variable with a uniform probability density function. The desired signal power at the output of the system shown in Figure 3 is again given by

$$P_s = \frac{A^2 C^2 T}{2} \quad (42)$$

but for the noise power, this time one obtains

$$P_n = 2FkT_0 \frac{C^2 T}{4} \quad (43)$$

Therefore, the signal-to-noise ratio at the output of this system is given by

$$(E/N) = P_s/P_n = \frac{A^2}{2} \cdot \frac{1}{kFT_0} \cdot T = S \cdot \frac{B_{if}}{N} \cdot T = (S/N)TB_{if} \quad (44)$$

with (S/N) as given in Equation (12).

This is the signal-to-noise ratio expression for a quadrature receiver after signal processing has been employed.

4. Pulsed source and incoherent pulse integration

This system is a typical range-gated radar utilizing a pulsed source. It may be used as a transmissometer by measuring the reflection from a calibrated corner reflector target. At the receiver, the signal is heterodyned to an intermediate frequency, then it is detected and then integrated with the use of a box-car device. A box-car device is a sample-and-hold circuit which stretches each pulse in time so as to cover the entire pulse repetition period. This device helps reduce harmonics of the pulse repetition frequency.

Since the receiver system employs post-detection integration rather than pre-detection (or coherent) integration, RF phase information is lost in the detection process. The non-linear nature of the detector creates a rectifying effect and harmonic distortion which reduces available signal power. If n pulses of the same signal-to-noise ratio were integrated by an ideal pre-detection integrator, after integration the resulting power signal-to-noise ratio would be exactly n times that of a single pulse. If post-detection integration is employed, however, a smaller signal-to-noise ratio would be observed. Thus, for the signal-to-noise ratio after integration, one can write

$$(E/N) = n' n \left(\frac{S}{N} \right), \quad (45)$$

where n' is the integration efficiency factor. The efficiency factor n' in Equation (45) is not the same as the efficiency factor n as Marcum[6] defines it. The defining equation in his work is

$$n = \frac{\left(\frac{S}{N} \right)_1}{\left(\frac{S}{N} \right)_n}, \quad (46)$$

where $(S/N)_1$ is the value of the signal-to-noise ratio of a single pulse required to yield a given probability of detection, and $(S/N)_n$ is the value of the signal-to-noise ratio of a single pulse required

to achieve the same probability of detection when n such pulses are integrated. This factor has been calculated by Marcum[6] and plotted by Skolnik[2]. The curves shown in Figure 5 are integration improvement factor $I = n$, and integration loss $L = 10 \log \left(\frac{1}{n} \right)$, both versus n , the number of pulses integrated.

Let $(S/N)_n$ in Equation (46) be equal to (S/N) in Equation (45). Since n such pulses, when integrated give the same probability of detection as one with a signal-to-noise ratio of $(S/N)_1$, this value should be approximately equal to the combined signal-to-noise ratio of n pulses, namely (E/N) in Equation (45). Thus, n' is approximately equal to n . Although the definition of efficiency used in this thesis and applied for the calculation of the processed signal-to-noise ratio does not involve probability of detection, i.e., it is assumed to be independent of this factor, the curves presented here are still applicable to the calculation of interest because a study of the curves reveals that the efficiency factor is not heavily dependent on the threshold level (i.e., the probability of detection). Since the primary purpose of the calculations was to find the range at which (E/N) has a value of 10 dB, the curve corresponding to $(S/N)_1 = 10$ dB in Figure 5 should be used. The curve for which false alarm number n_f is 10^4 and probability of detection P_d is 0.50 is such a curve. Thus, using Equations (45) and (12), one obtains

$$(E/N) = \frac{P_t G_t G_r \lambda^2 \sigma L_t L_r n' n}{(4\pi)^3 R^4 k T_0 B F} 10^{-2\alpha R/10} \quad , \quad (47)$$

where n' may be determined using Figure 5.

5. Pulsed source and quadrature receiver

This system also is a radar with a pulsed source. The receiver is a quadrature receiver as shown in Figure 3. This time however, the receiver is range-gated, i.e., the multiplier input shown in Figure 4a is given by

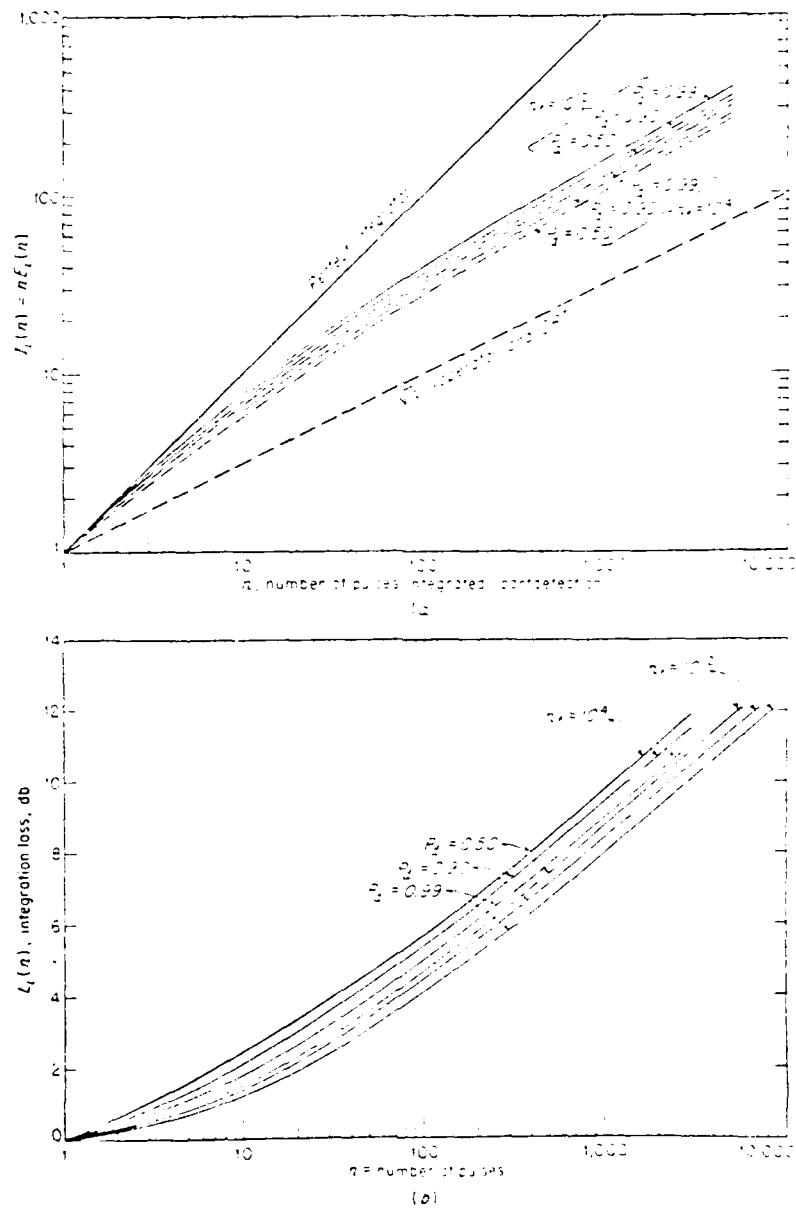


Figure 5. a) Integration improvement factor,
b) Integration loss,
versus number of pulses integrated.

$$s(t) = C \cos \omega_c t p(t) \quad (48)$$

where $p(t)$ is a train of pulses of width τ , separation T_r , which are contained in the time interval $(0, T)$. The desired signal output at $t=T$ is given by

$$y(T) = \int_0^T r(t)p(t)s(t) dt = \frac{ACTd}{2} \quad (49)$$

so that the desired signal power is

$$P_s = \left(\frac{ACTd}{2} \right)^2 \quad (50)$$

where d is the duty cycle of the signal given by

$$d = \frac{\tau}{T_r} \quad (51)$$

Again, if T , T_r and τ are chosen conveniently, the impulse response of the equivalent filter of Figure 4b is given by

$$h(t) = C \cos \omega_c t p(t) \quad (52)$$

If the filter were matched to only one RF pulse of duration τ , following the derivation of Equation (40), for the noise power at the output, one obtains

$$P_\tau = \frac{FkT_0 C^2 \tau}{4} \quad (53)$$

Thus, for the noise power at the output of the filter with its impulse response as given in Equation (52), one obtains

$$P_n = \frac{FkT_0 C^2 \tau n}{4} \quad (54)$$

where n is the number of pulses integrated given by

$$n = \frac{T}{T_r} \quad (55)$$

Using Equations (50), (51), (54) and (55), and following the same argument leading to Equation (44), for the signal-to-noise ratio at the output of the range-gated version of the system shown in Figure 3, one obtains

$$(E/N) = (S/N) T B_{if} d \quad (56)$$

where (S/N) is as given in Equation (12).

C. Attenuation Due to Rain and Fog

The path attenuation parameter α appearing in Sections A and B of this Chapter has a value of approximately 0.3 dB/km [1] near 94 GHz at sea level in clear air. This attenuation is due primarily to molecular absorption by oxygen and water vapor. The attenuation increases very markedly during rain and possibly during fog. What was sought here was therefore an expression for attenuation effects on the path of propagation due to rain or fog. Rain and fog are assumed to consist of spherical water droplets of complex refractive index to account for dissipation and scattering of electromagnetic energy. Scattering from a sphere has been studied by Mie[7], and the theory is reviewed by Kerker[8]. Appendix A gives pertinent parts of the theory cast into a more modern form with the use of vector and scalar potentials.

The attenuation factor caused by a density of spherical droplets may be found using a first order approximation through [9]

$$\alpha = 4.343 \int_0^\infty C_{EXT}(a) N(a) da \quad (57)$$

where α is the specific attenuation in (dB/m), a is the radius of the droplets in (m), N is the density of droplets with radius a in $\frac{1}{m^3 \cdot m}$ and Q_{EXT} is the extinction efficiency factor given by Equation (A59) in Appendix A.

D. Summary

The signal-to-noise ratio expressions before signal processing have been derived in Section II.A for two-ended systems and radar type systems as given in Equations (7) and (12).

In Section II.B, expressions for signal-to-noise ratio for five types of instrumentation have been given by Equations (15), (44), (47) and (56). The pre-detection signal-to-noise ratios $(S/N)_{if}$ in these equations are those derived in Section II.A.

In Section II.C, Equation (57) gives the specific attenuation due to rain or fog, as a function of drop size distribution, for use in the equations developed in Section II.A.

SECTION III

RESULTS

A. System Calculations

Values of the processed signal-to-noise ratio were calculated as a function of range for the five types of instrumentation. The range R was varied from 500 meters to 8 kilometers in 100 meter steps, and the appropriate one of the Equations (15), (44), (45) or (56) and (7) or (12) in Section II were used. In the calculations, the propagation path is assumed to be uniform or to consist of horizontal layers of homogeneous specific attenuation each; in the latter case, the overall effect of these layers is taken into account by replacing (αR) in Equations (7) or (12) by $\sum_i \alpha_i R_i$, where α_i is the specific attenuation of the i th layer and R_i is the one-way length of the path through the i th layer.

Also, routines were developed to calculate and plot maximum attainable range as a function of the specific attenuation α . First, the value of the signal-to-noise ratio was calculated using one of Equations (15), (44), (45) or (56) for a processed signal-to-noise ratio of 10 dB. Then, α was varied from 30 dB/km to 0 in -0.1 dB/km steps. Using Equation (7) the following equation was obtained and used for iterations to solve for R

$$R_{n+1} = \frac{10}{\alpha} \left\{ \log_{10} \left[\frac{P_t G_t G_r^2 L_t L_r}{(4\pi)^2 k T_0 B F(S/N)} \right] - 2 \log_{10} R_n \right\}, \quad (58)$$

where S/N is that signal-to-noise ratio at the output of the intermediate frequency amplifier which yields a processed signal-to-noise

ratio of 10 dB. Similarly, for systems of the radar type, by use of Equation (12), one obtains

$$R_{n+1} = \frac{10}{2\alpha} \left\{ \log_{10} \left[\frac{P_t G_t G_r^2 L_t L_r}{(4\pi)^3 k T_0 B F(S/N)} \right] - 4 \log_{10} R_n \right\} \quad (59)$$

For $\alpha=30$ dB/km, the iterations were started with $R_0=1$ m. For other values of α , the solution corresponding to the preceding α value $R(\alpha+0.1)$ was used for R_0 . The iterations were stopped when $R_{n+1}-R_n \leq 1$ m. This method was found to converge for large values of α . A different method was used for smaller values of α , with which the first scheme (defined by Equations (58) and (59)) fails. This was tested by looking for unreasonably large values of R . For this case, the R appearing in the denominator in Equation (7) was used on the left-hand side, leading to the equation used for the iterations to solve for the range for the two-ended system

$$R_{n+1} = \sqrt{\frac{P_t G_t G_r^2 L_t L_r}{(4\pi)^2 k T_0 B F(S/N)}} 10^{-\alpha R_n/20} \quad (60)$$

Similarly, for systems of the radar type, Equation (12) leads to

$$R_{n+1} = 4 \sqrt{\frac{P_t G_t G_r^2 L_t L_r}{(4\pi)^3 k T_0 B F(S/N)}} 10^{-2\alpha R_n/40} \quad (61)$$

Again, $R(\alpha+0.1)$ was taken for the first value of R to be used on the right-hand side of the equation and the same test as for large α was made to stop the iterations.

Throughout the calculations, the following values were used:

$$G_t = 47 \text{ dB},$$

$$G_r = 53 \text{ dB}$$

$$P_t = 200 \text{ mW}$$

$$L_t + L_r = 11 \text{ dB},$$

$$F = 9 \text{ dB},$$

$$\sigma = 125 \text{ m}^2 \text{ (when applicable),}$$

where all the symbols carry the same meanings defined in Section II.A. The gain values correspond to 12" and 24" diameter parabolics. The transmitted power value is typical of an IMPATT diode source. The calibrated target is a corner reflector; this, as well as the system loss and noise figure values correspond to a reasonable experimental system. These parameters are inputs read by the programs which would run equally well with different values. They can be changed easily.

B. Results and Discussions

Figures 6 through 9 relate to the system with physically separate transmitter and receiver and with a square-law detector at the receiver end (Section II.B.1). In all of these figures, B_a , the audio filter bandwidth is 1 Hz. Figures 6, 7 and 8 show signal-to-noise ratio versus range for different values of B_{if} with α , the specific attenuation, as a parameter. It may be observed from these curves that as α increases, the signal-to-noise ratio E/N , at the system output not only decreases, but its rate of decrease with respect to R increases very much. The parameter B_{if} does not affect the E/N values much for small R , but decreasing this parameter will yield better E/N values for large R . Figure 9 shows the variation of R as a function of α for an E/N value of 10 dB. Even under severe weather conditions, a range of 3 to 4 kilometers can be achieved.

Figures 10, 11 and 12 show the curves of signal-to-noise ratio E/N versus range for a single-ended system with the receiver identical to that of the previous system (Section II.B.2) for $B_{if} = 100$ KHz, 10 MHz, 1 GHz. Figure 13 is a graph of range versus specific attenuation for the same systems for $E/N=10$ dB. Again, the signal-to-noise ratio is sensitive to B_{if} only for large values of R . Comparing Figures 10, 11 and 12 to the corresponding figures for the previous system, one can observe that this system is much more sensitive to α . The performance of the system drops very rapidly for $\alpha=5$ dB/km compared

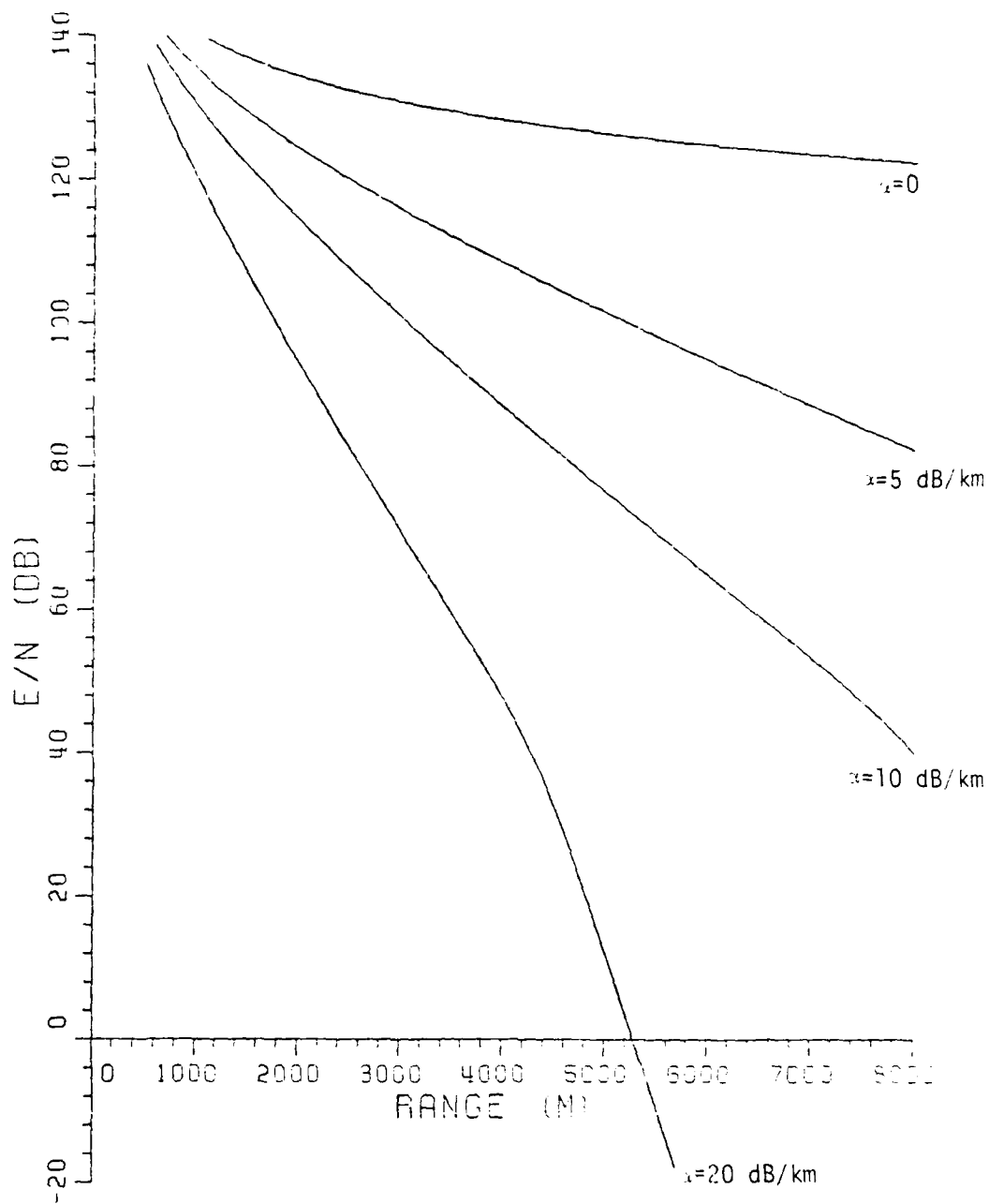


Figure 6. Signal-to-noise ratio versus range for the two-ended system with square-law detector. Intermediate frequency bandwidth $B_{if}=100$ KHz, audio filter bandwidth $B_a=1$ Hz. α : specific attenuation.

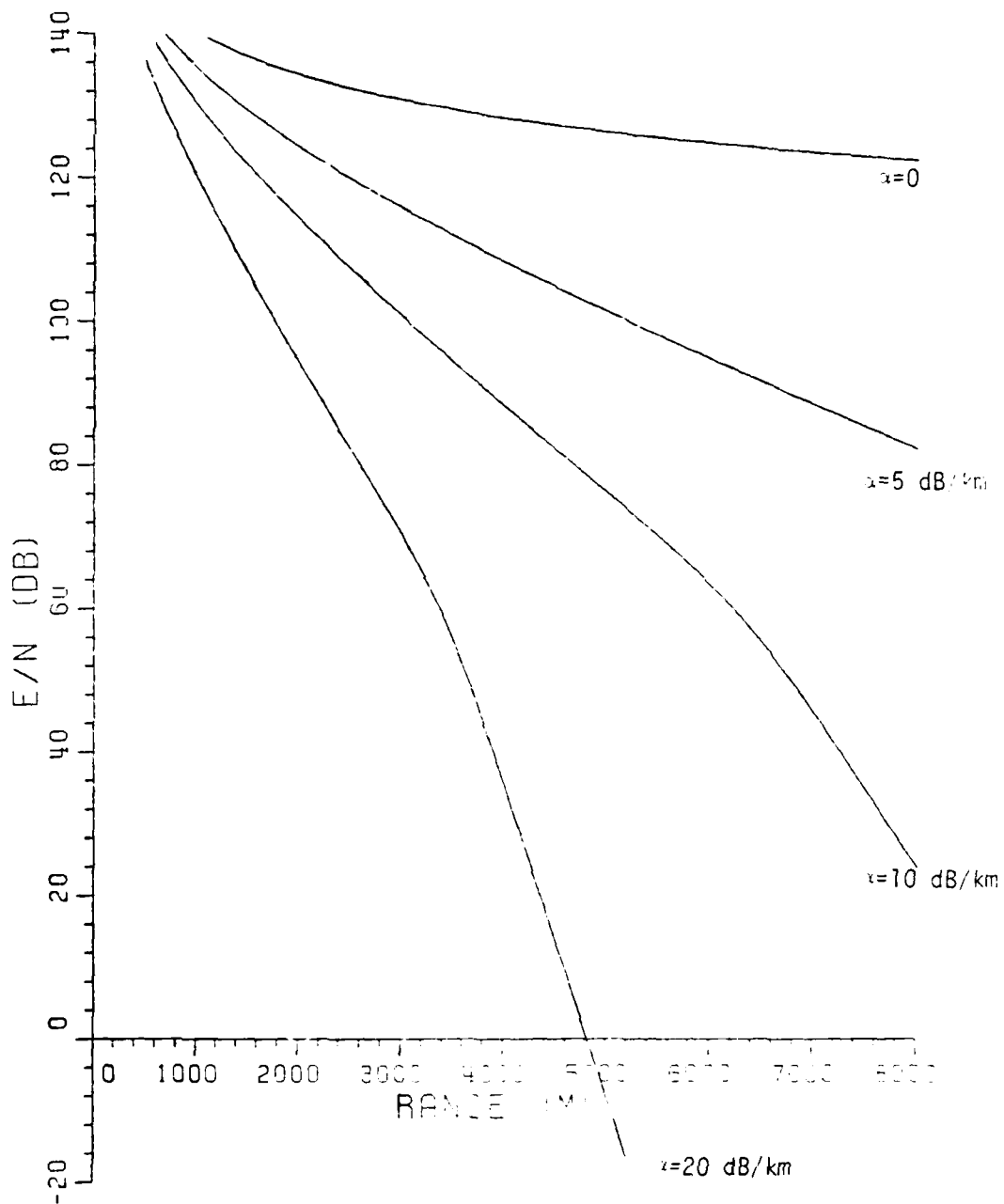


Figure 7. Signal-to-noise ratio versus range for the two-ended system with square-law detector. Intermediate frequency bandwidth $B_{if}=10$ MHz, audio filter bandwidth $B_a=1$ Hz. α : specific attenuation.

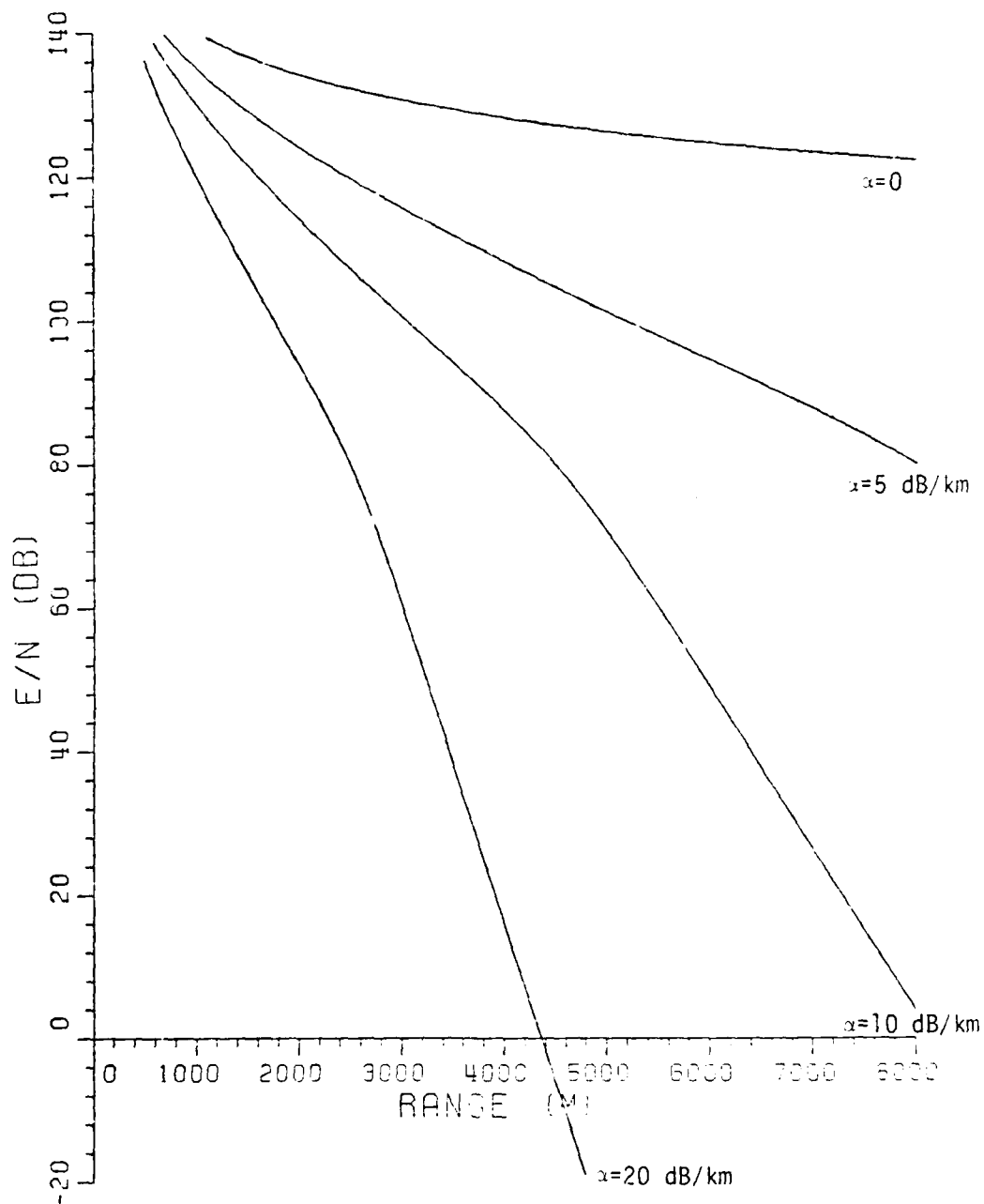


Figure 8. Signal-to-noise ratio versus range for the two-ended system with square-law detector. Intermediate frequency bandwidth $B_{if}=1$ GHz, audio filter bandwidth $B_a=1$ Hz. α : specific attenuation.

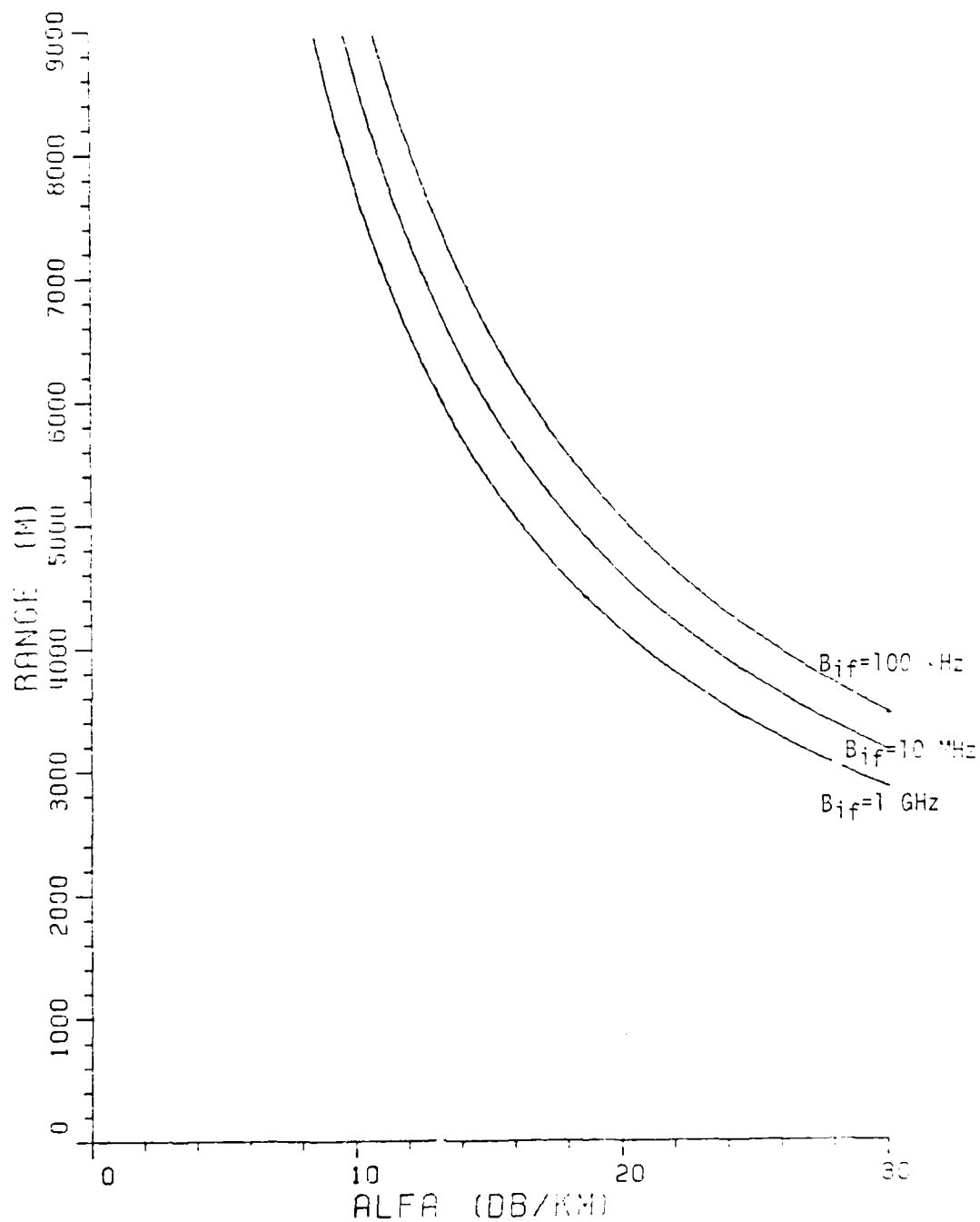


Figure 9. Range versus specific attenuation for $E/N=10$ dB for the two-ended system with square-law detector. Audio filter bandwidth $B_a=1$ Hz. B_{if} : Intermediate frequency bandwidth.

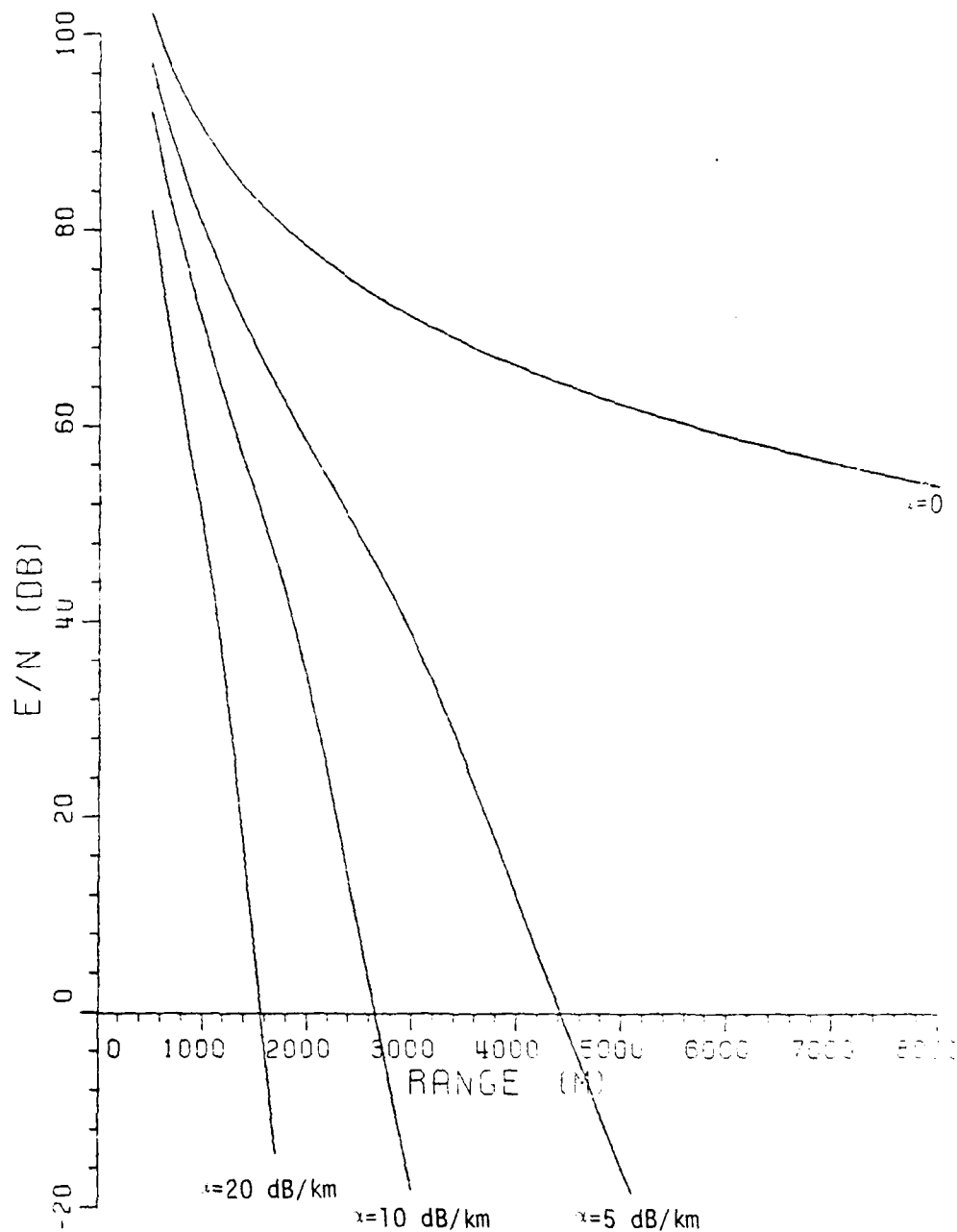


Figure 10. Signal-to-noise ratio versus range for the single-ended system with square-law detector. Intermediate frequency bandwidth $B_{if}=100$ KHz, audio filter bandwidth $B_a=1$ Hz. α : specific attenuation.

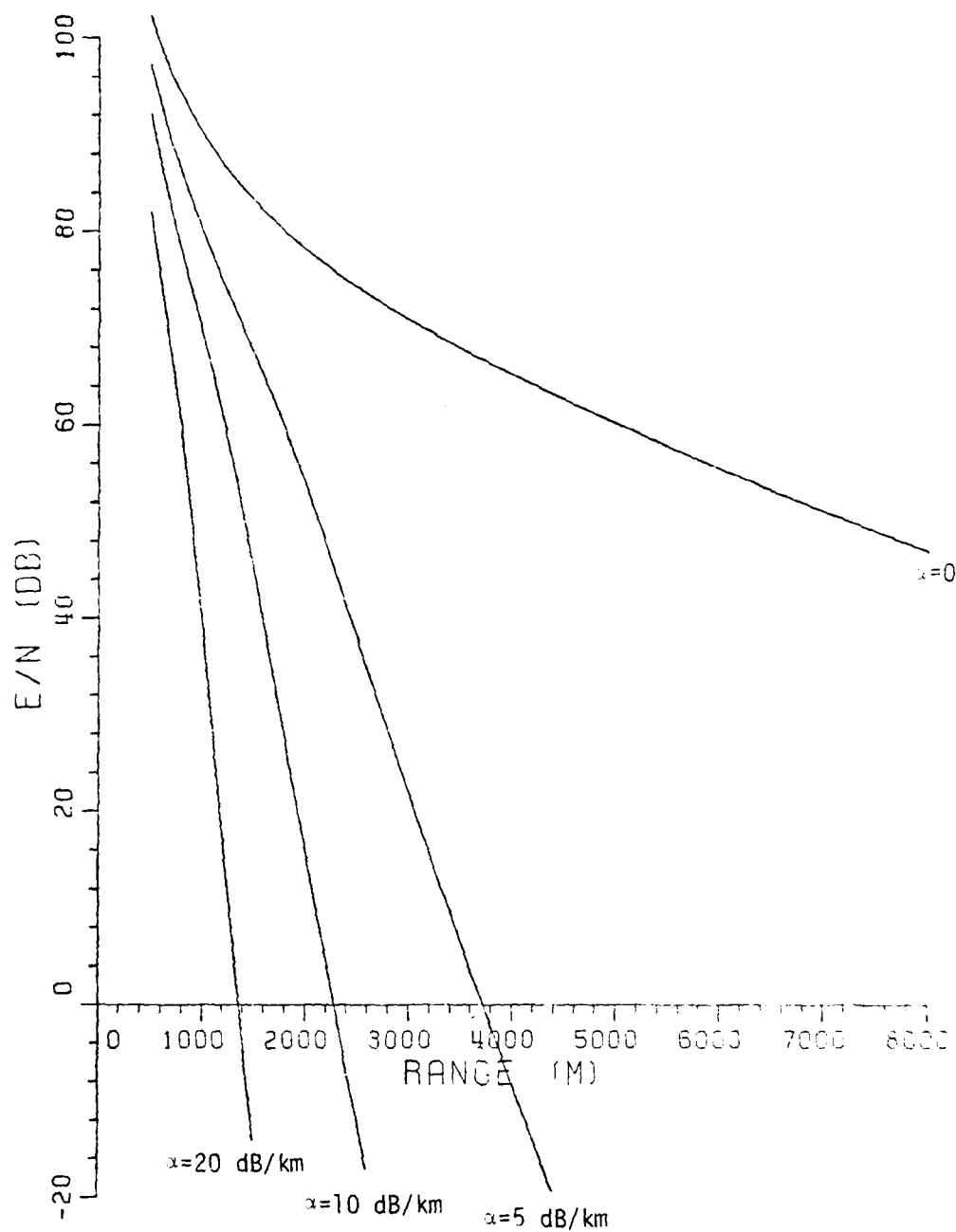


Figure 11. Signal-to-noise ratio versus range for the single-ended system with square-law detector. Intermediate frequency bandwidth $B_{if}=10$ MHz, audio filter bandwidth $B_a=1$ Hz. α : specific attenuation

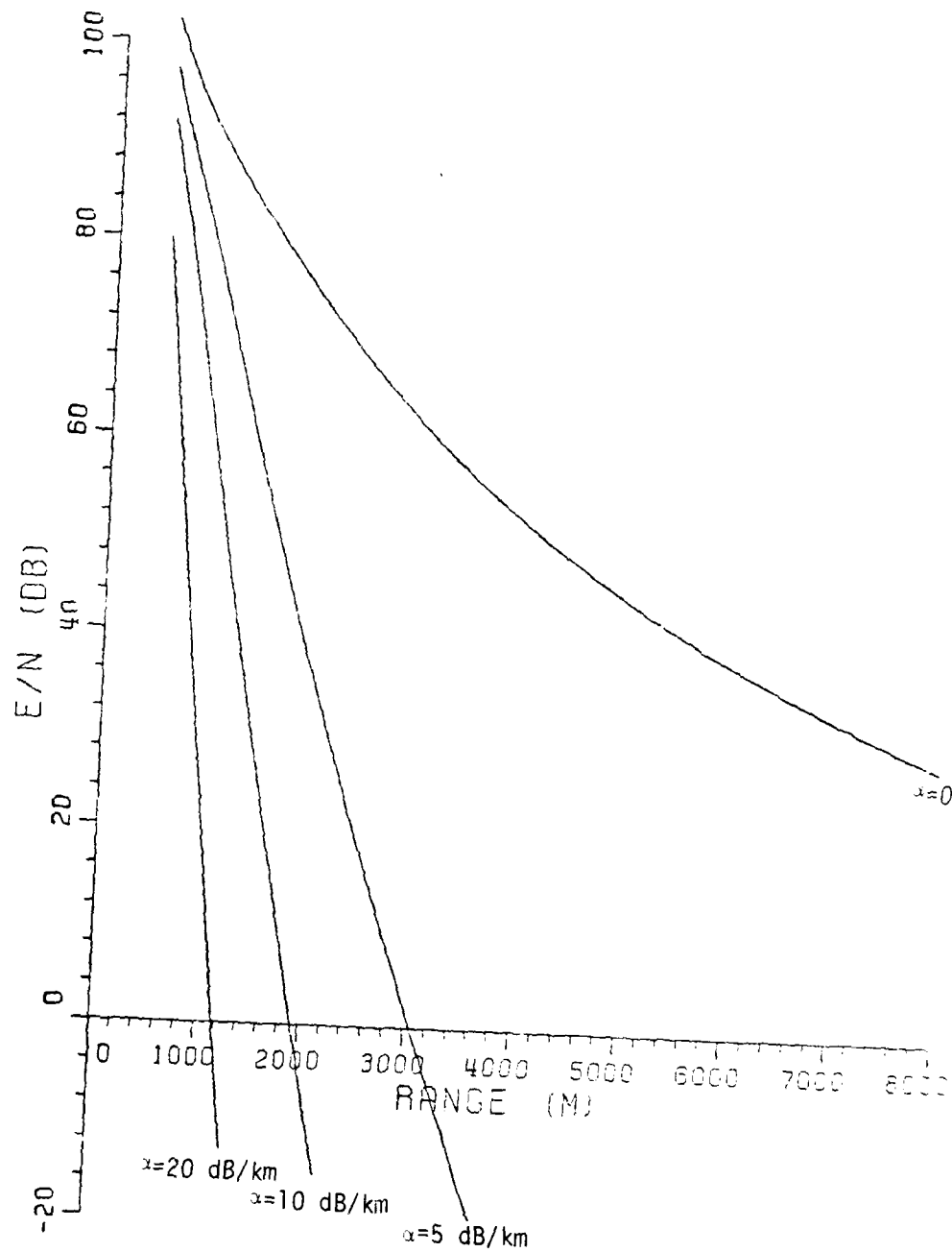


Figure 12. Signal-to-noise ratio versus range for the single-ended system with square-law detector. Intermediate frequency bandwidth $B_{if}=1$ GHz, audio filter bandwidth $B_a=1$ Hz. α : specific attenuation.

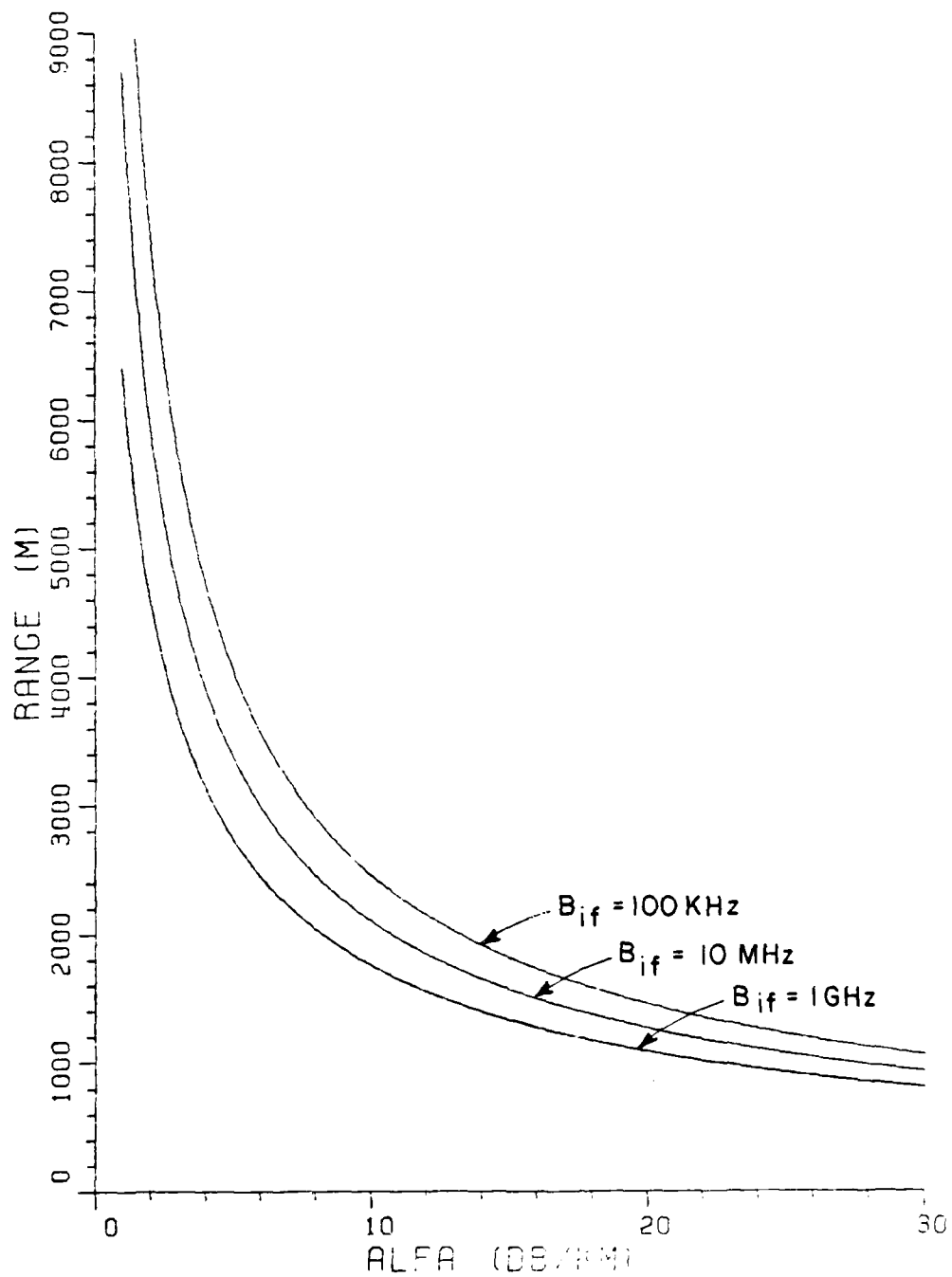


Figure 13. Range versus specific attenuation for $E/N=10$ dB for the single-ended system with square-law detector. Audio filter bandwidth $B_a=1$ Hz. B_{if} : Intermediate frequency bandwidth.

to $\alpha=0$. Under heavy weather conditions, the attainable range is only 1000 to 1500 meters.

Figures 14, 15, 16 and 17 show results for the single-ended system with continuous wave transmission and with a quadrature receiver (Section II.B.3). They also represent the similar system with a pulsed source (Section II.B.5) if the duration of integration T is replaced by Td where d is the duty cycle. Again, the first three figures show E/N versus range and the last one shows range versus α for the E/N value of 10 dB. As seen in Figure 17, a range of approximately 2 kilometers can be achieved with severe weather conditions.

Figures 18, 19, 20 and 21 show E/N versus range, and range versus α curves for the single-ended system which employs post-detection integration (Section II.B.4). In the first three figures, the value of n , the number of pulses integrated, are different. For all the curves, the intermediate frequency bandwidth is 10 MHz. As is seen in Figure 21, a range of approximately 1 km can be achieved with high attenuation.

Assuming the intermediate frequency bandwidth figure of 10 MHz to be typical for the receiver with the square-law detector, and since the value of 1 Hz for the audio filter bandwidth requires the signal to be processed for approximately 1 second, Figures 11 and 14 are the curves to compare the performances of the single-ended systems with quadrature and square-law detectors. It may be observed from these figures that the system with the quadrature receiver is much superior especially for large R and large α values. This is expected, because for the system with the quadrature receiver, the processed signal-to-noise ratio is proportional to the signal-to-noise ratio at the output of the i.f. filter as seen in Equation (44); whereas for the system with a square-law detector, the final signal-to-noise ratio will be smaller,

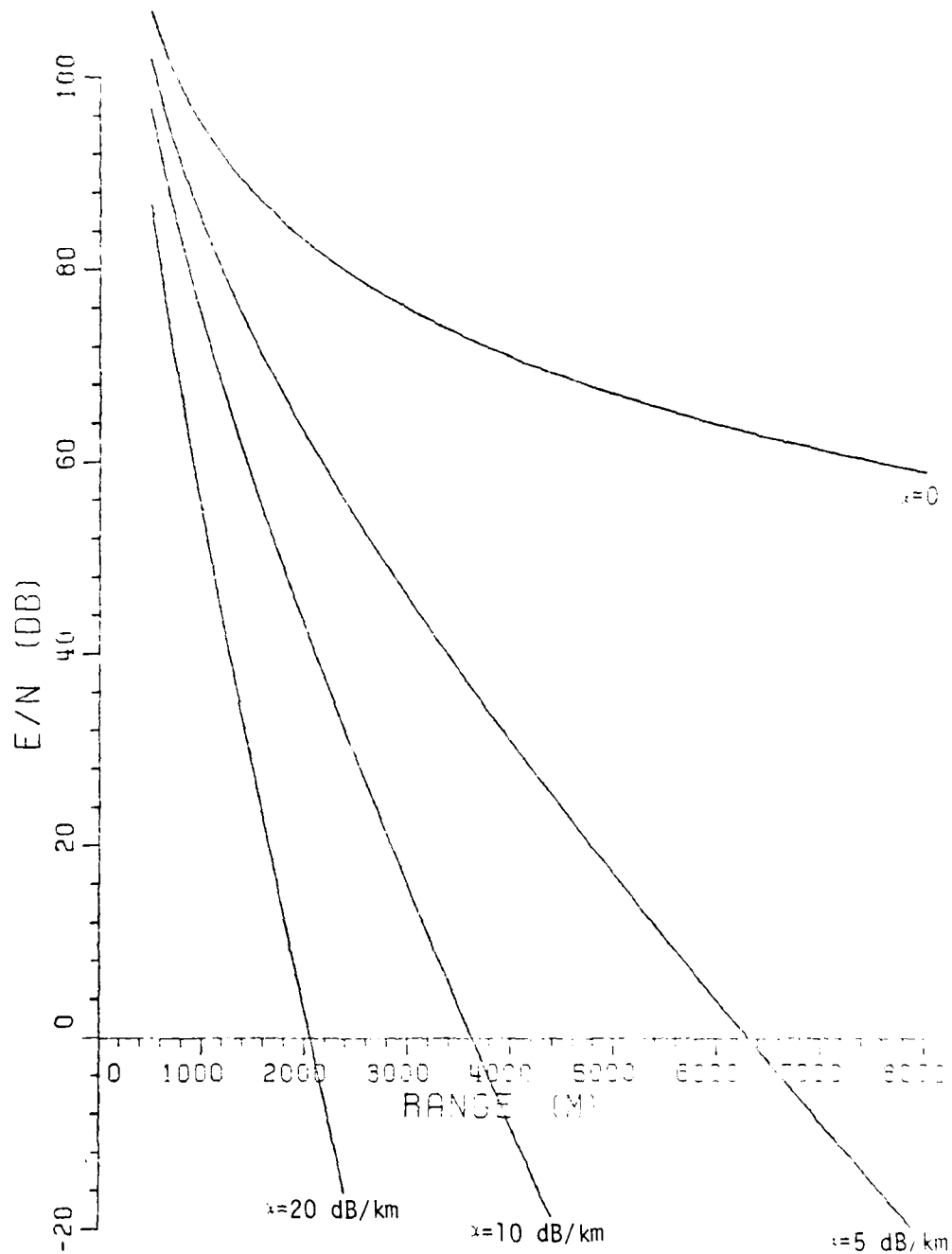


Figure 14. Signal-to-noise ratio versus range for the single-ended system with quadrature receiver. Integration time $T=1$ sec. α : specific attenuation.

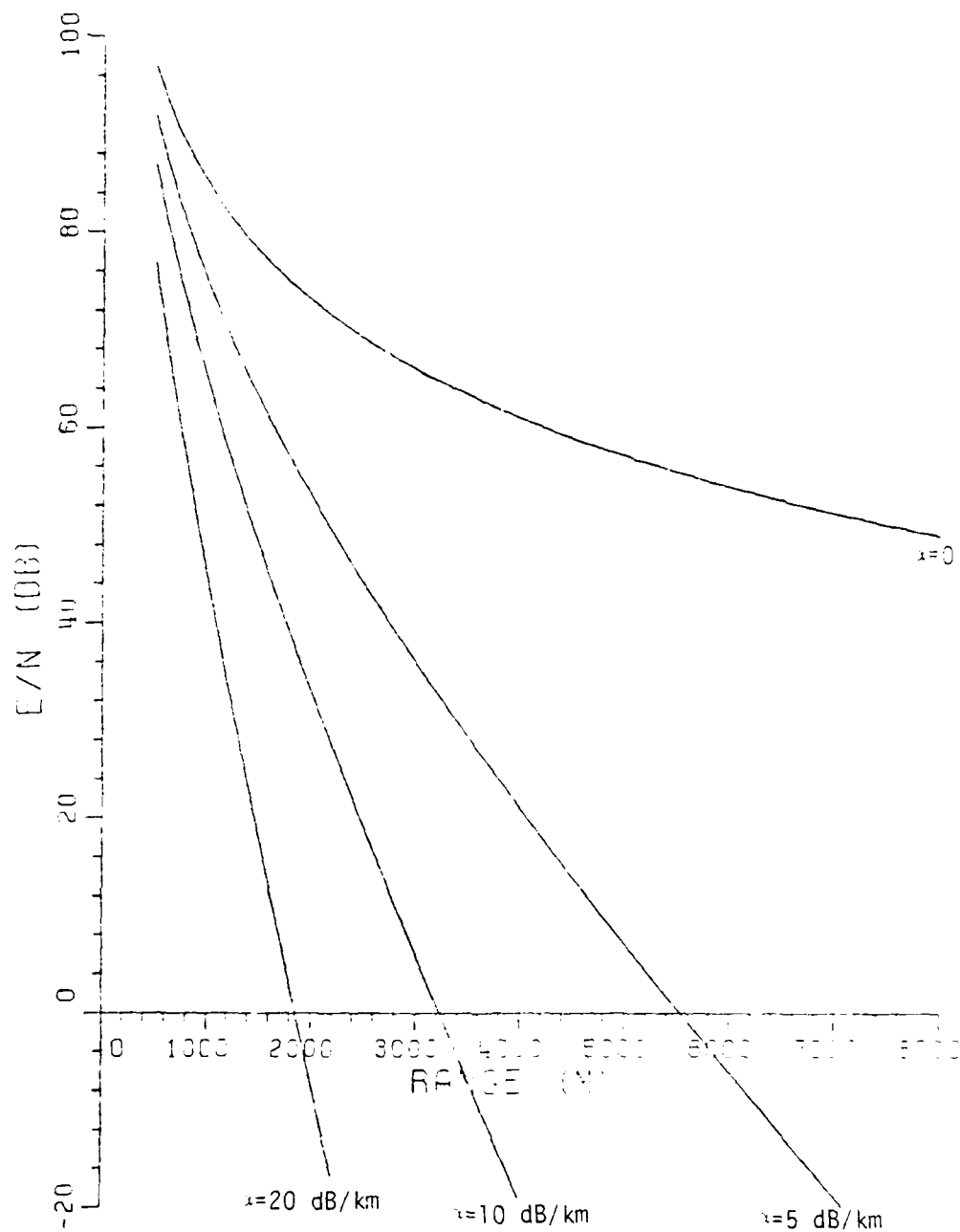


Figure 15. Signal-to-noise ratio versus range for the single-ended system with quadrature receiver. Integration time $T=0.1$ sec. α : specific attenuation.

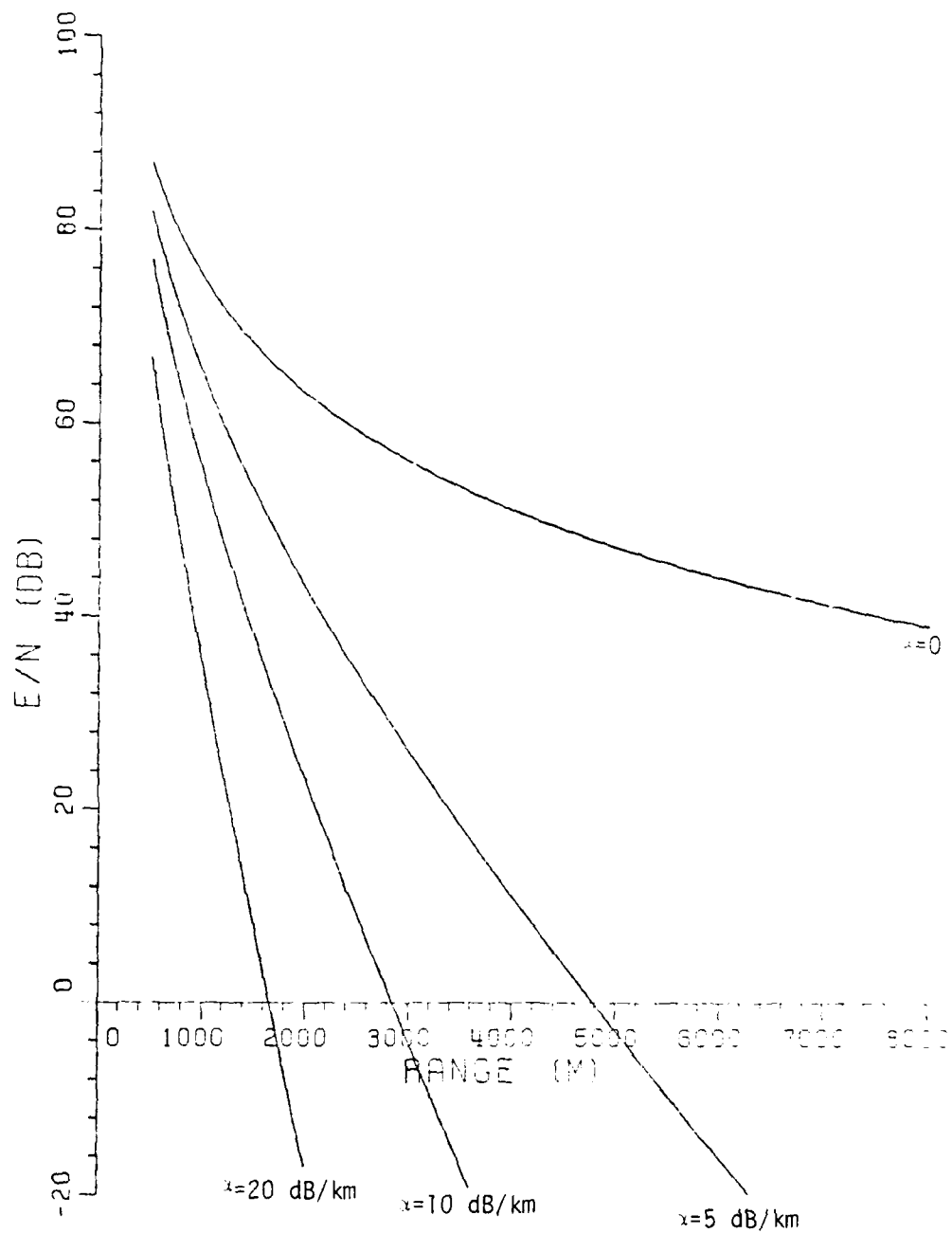


Figure 16. Signal-to-noise ratio versus range for the single-ended system with quadrature receiver. Integration time $T=0.01$ sec. α : specific attenuation.

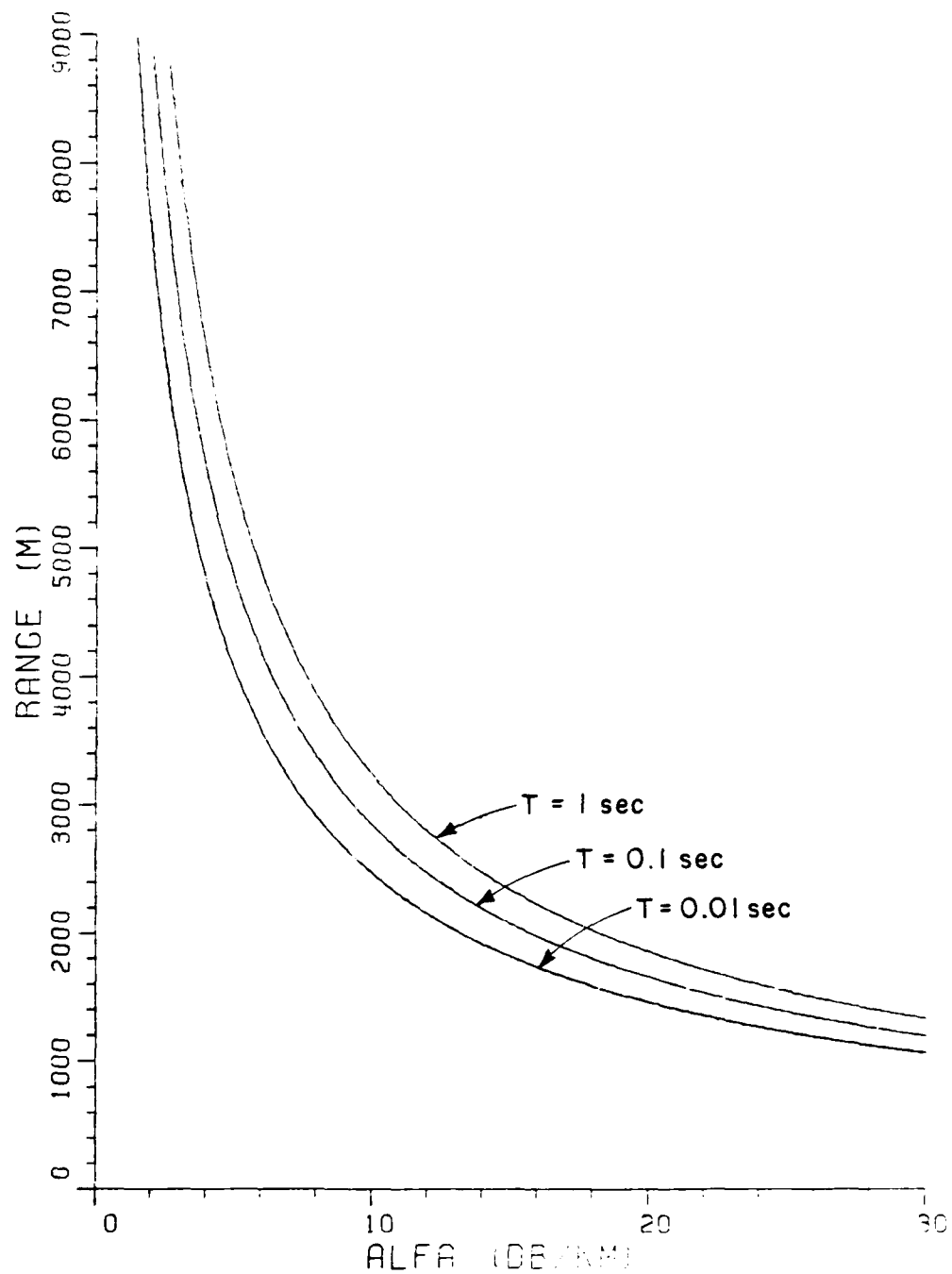


Figure 17. Range versus specific attenuation for $E/N=10 \text{ dB}$ for the single-ended system with quadrature receiver. T : integration time.

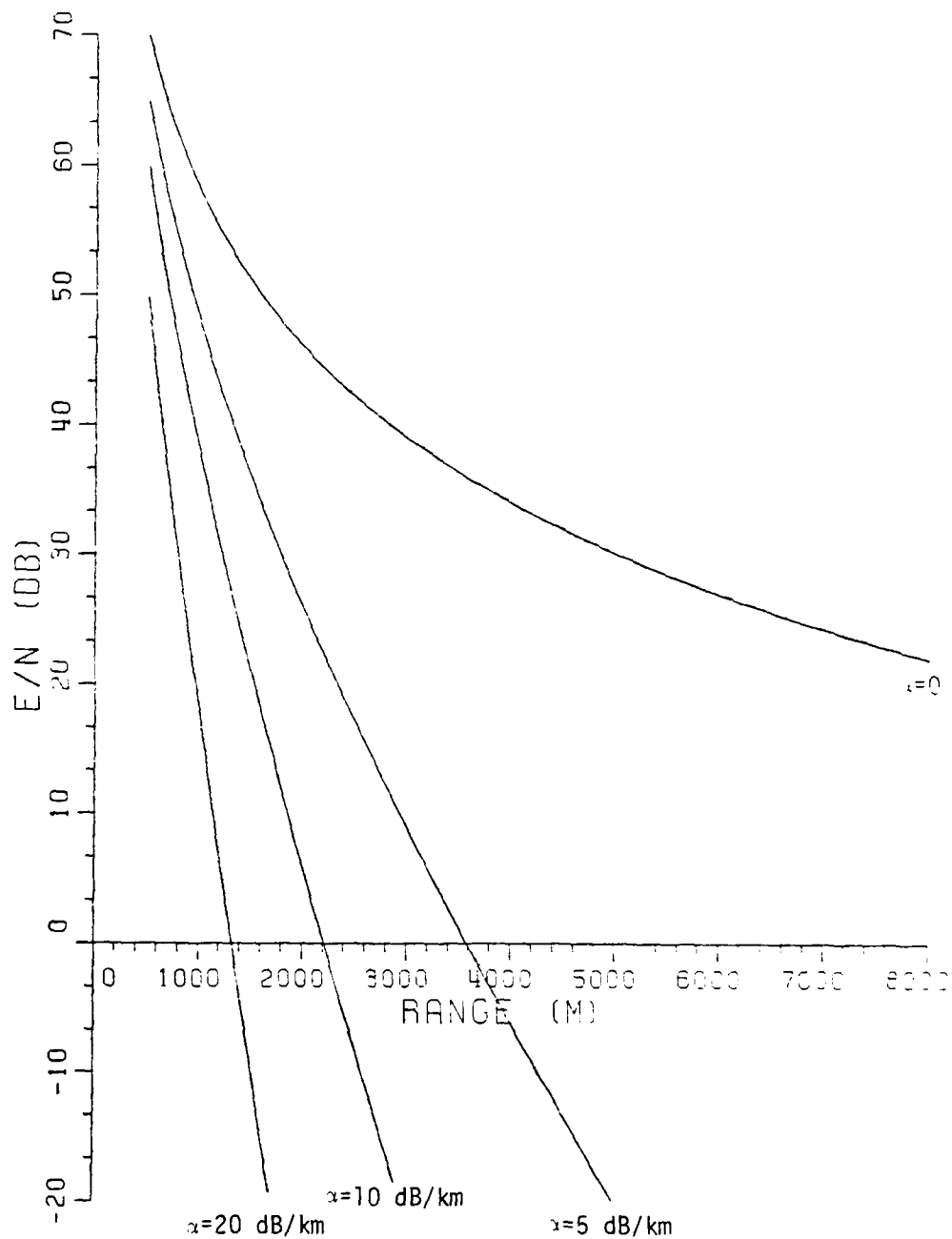


Figure 18. Signal-to-noise ratio versus range for the single-ended system employing post-detection integration. Intermediate frequency bandwidth $B_{if}=10$ MHz, number of pulses $n=100000$. α : specific attenuation.

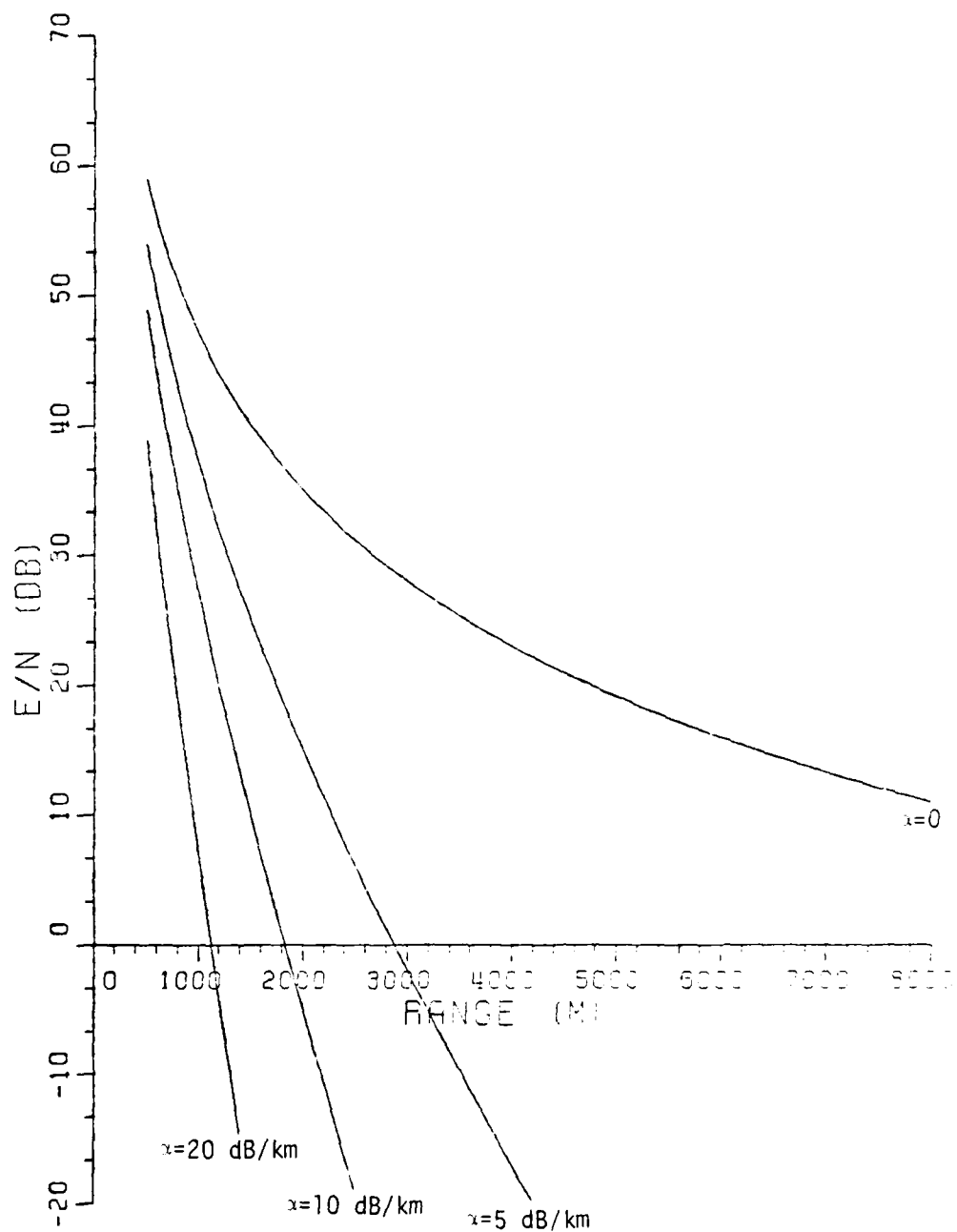


Figure 19. Signal-to-noise ratio versus range for the single-ended system employing post-detection integration. Intermediate frequency bandwidth $B_{if}=10$ MHz, number of pulses $n=1000$. α : specific attenuation.

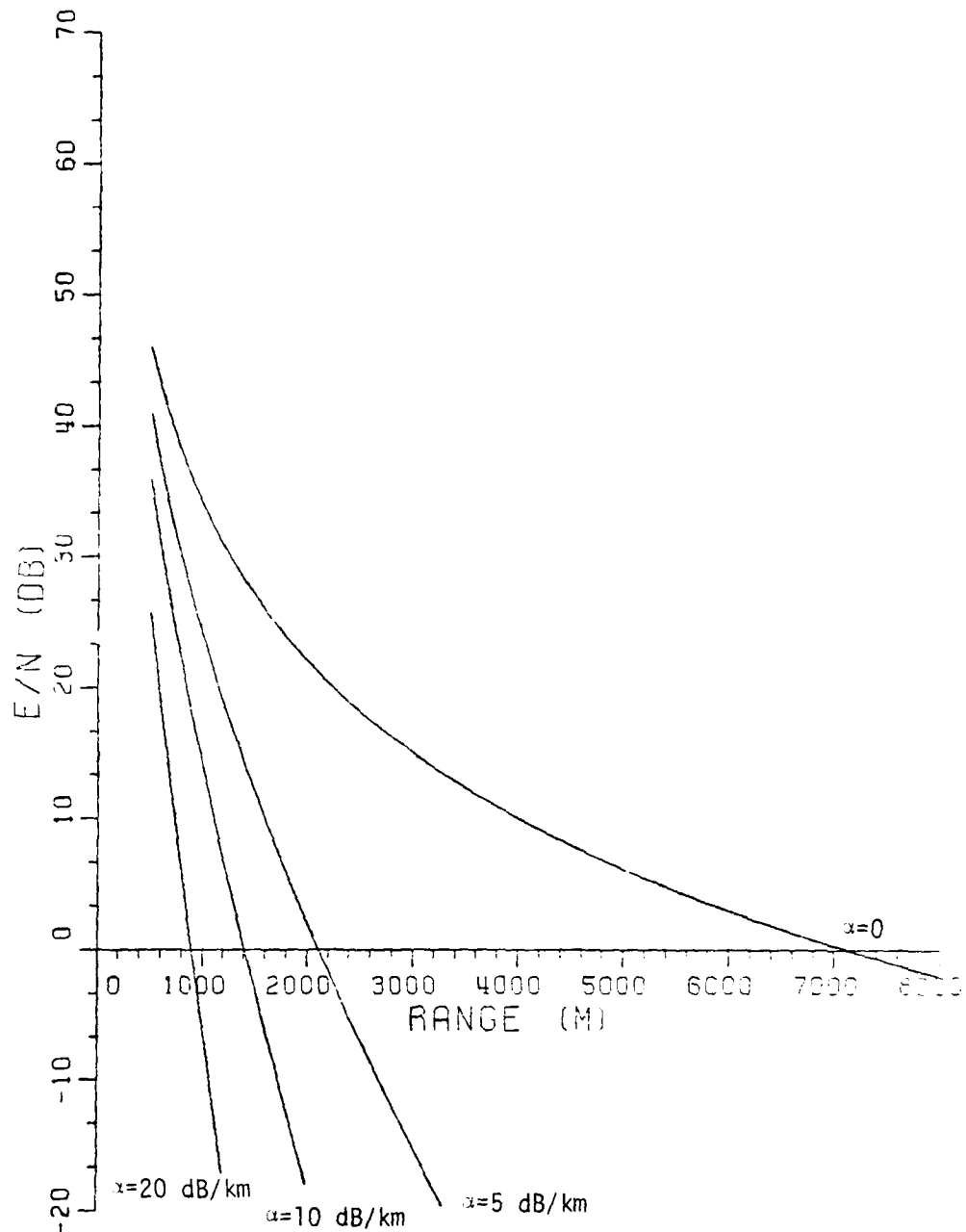


Figure 20. Signal-to-noise ratio versus range for the single-ended system employing post-detection integration. Intermediate frequency bandwidth $B_{if}=10$ MHz, number of pulses $n=10$. α : specific attenuation.

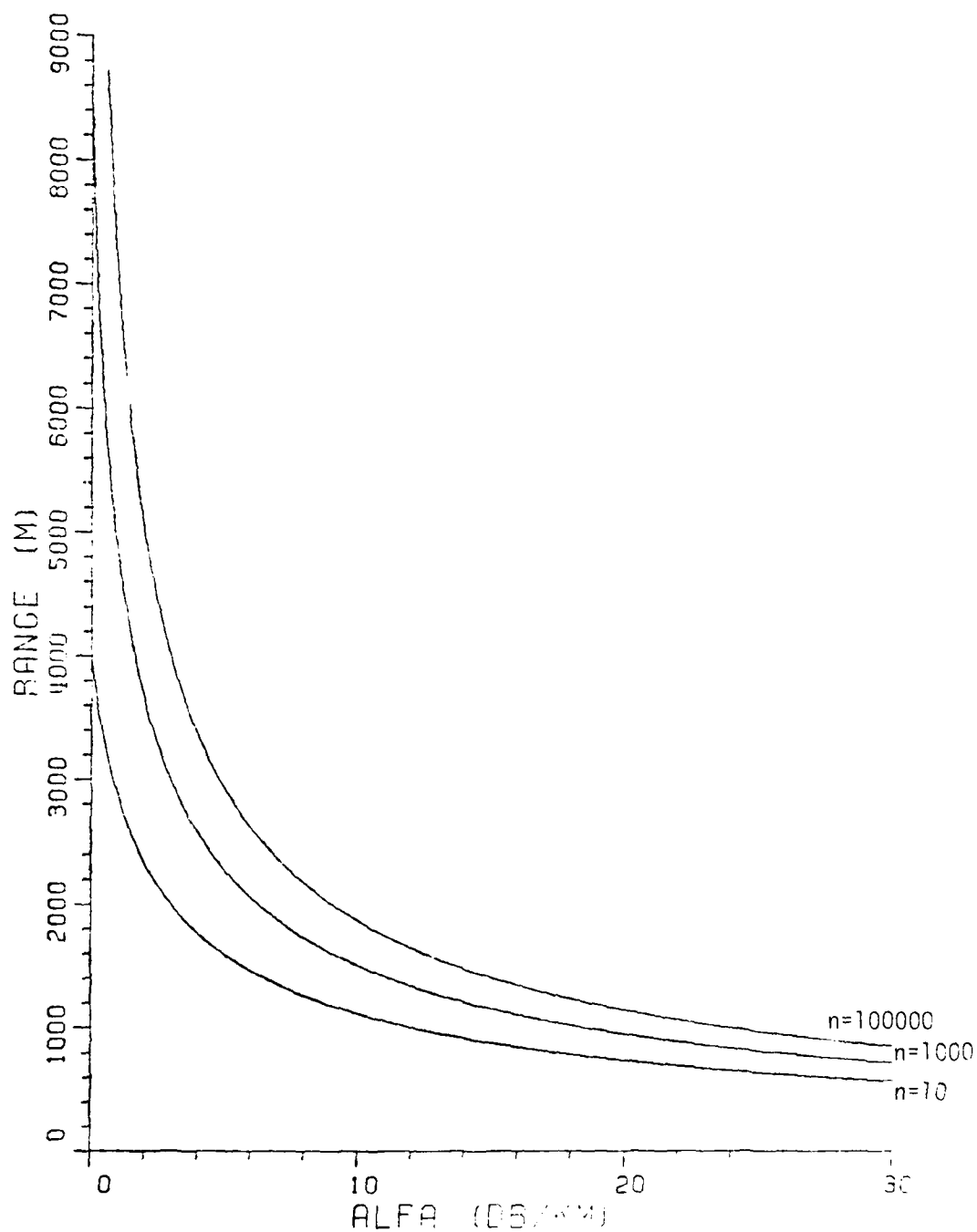


Figure 21. Range versus specific attenuation for $E/N=10$ dB for the single-ended system employing post-detection integration. Intermediate frequency bandwidth $B_{if}=10$ MHz. n : number of pulses.

as can be observed from Equation (15), especially for small values of unprocessed signal-to-noise ratio corresponding to large R or λ .

To compare the two radar-type systems with pulsed sources, consider first the curves in Figure 18. The i.f. bandwidth is 10 MHz which implies a pulse width of approximately 10^{-7} seconds. Assuming a duty cycle of 0.01, this would lead to a pulse repetition period of 10^{-5} seconds. Since 100,000 pulses are integrated, the entire processing would take 1 second. The curves for the single-ended system with a quadrature receiver with an integration duration of 1 second and a duty cycle of 0.01 are shown in Figure 16. The system with the quadrature receiver does better than the one which employs post-detection integration as is expected following the argument given in Section II.B.4.

Another observation that can be made from the curves presented here is that changing system parameters such as duration of integration, number of pulses, target cross section area, etc. prove to be of more value in attaining larger signal-to-noise ratio for given range than in attaining greater range for given signal-to-noise ratio. This is expected from Equations (7) and (12). It can be observed from these equations that range for fixed signal-to-noise ratio is less dependent on these parameters than is signal-to-noise ratio for fixed range. Signal-to-noise ratio is generally a linear function of these variables. Range, however behaves as a square-root function for the two-ended system and a fourth-root function for radar type systems in clear air. When attenuation is high, the exponential terms in Equations (7) and (12) become dominant and the range is proportional to the logarithm of the parameter in question for single-ended systems and half the logarithm for the two-ended system.

It is the less sensitive dependence of signal-to-noise ratio on range and specific attenuation that gives the two-ended system an

advantage which can be only partially offset by employing coherent detection with a single-ended configuration.

It is also of interest to see how a pulsed radar with pulses of 1 kW peak power would perform. Figure 22 shows range versus specific attenuation for a radar system with a quadrature receiver. Figure 23 is for a radar system with post-detection integration. Except for transmitted power, all pertinent parameters are the same as those given on page 23. It can be observed that with the quadrature receiver, one can obtain ranges better than the pulse integration receiver by about 500 meters. In both systems, a range improvement of 500 meters to 1 km is observed for α values of 15 to 30 dB/km due to the improvement in transmitted power from 200 mW to 1 kW.

C. Rain Attenuation

Another computer program developed in this study is a subroutine which returns the value of specific attenuation for a given rain rate. The rain drop size distribution was assumed to be exponential, given by [10]

$$N(D) = N_0 e^{-\Lambda D} \text{ [drops/(m}^3 \cdot \text{mm)]} , \quad (62)$$

where

$$\begin{aligned} \Lambda &= \alpha r^\beta \text{ (mm}^{-1}\text{)}, \\ N_0 &= 8000 \text{ [drops/(m}^3 \cdot \text{mm)]}, \\ \alpha &= 4.1, \\ \beta &= -0.21 \end{aligned}$$

where r is the rain rate in mm/Hr and D is the droplet diameter in mm. The rain water refractive index was taken to be [11]

$$n_c = 2.2 - j0.74 .$$

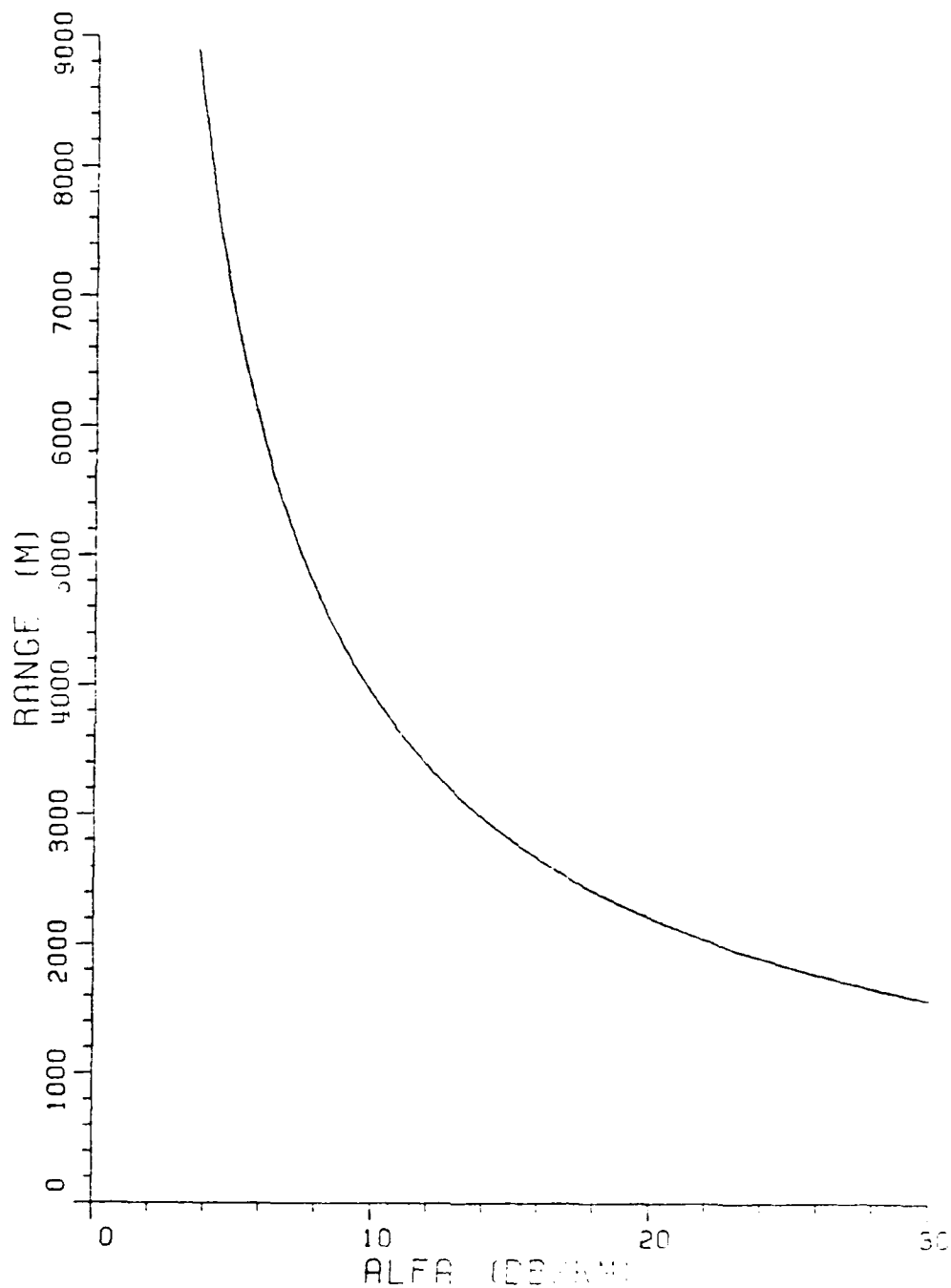


Figure 22. Range versus specific attenuation for $E/N=10$ dB for the radar system with quadrature receiver. Power transmitted $P_t=1$ Kw, integration time $T=1$ sec, duty cycle $d=0.01$.

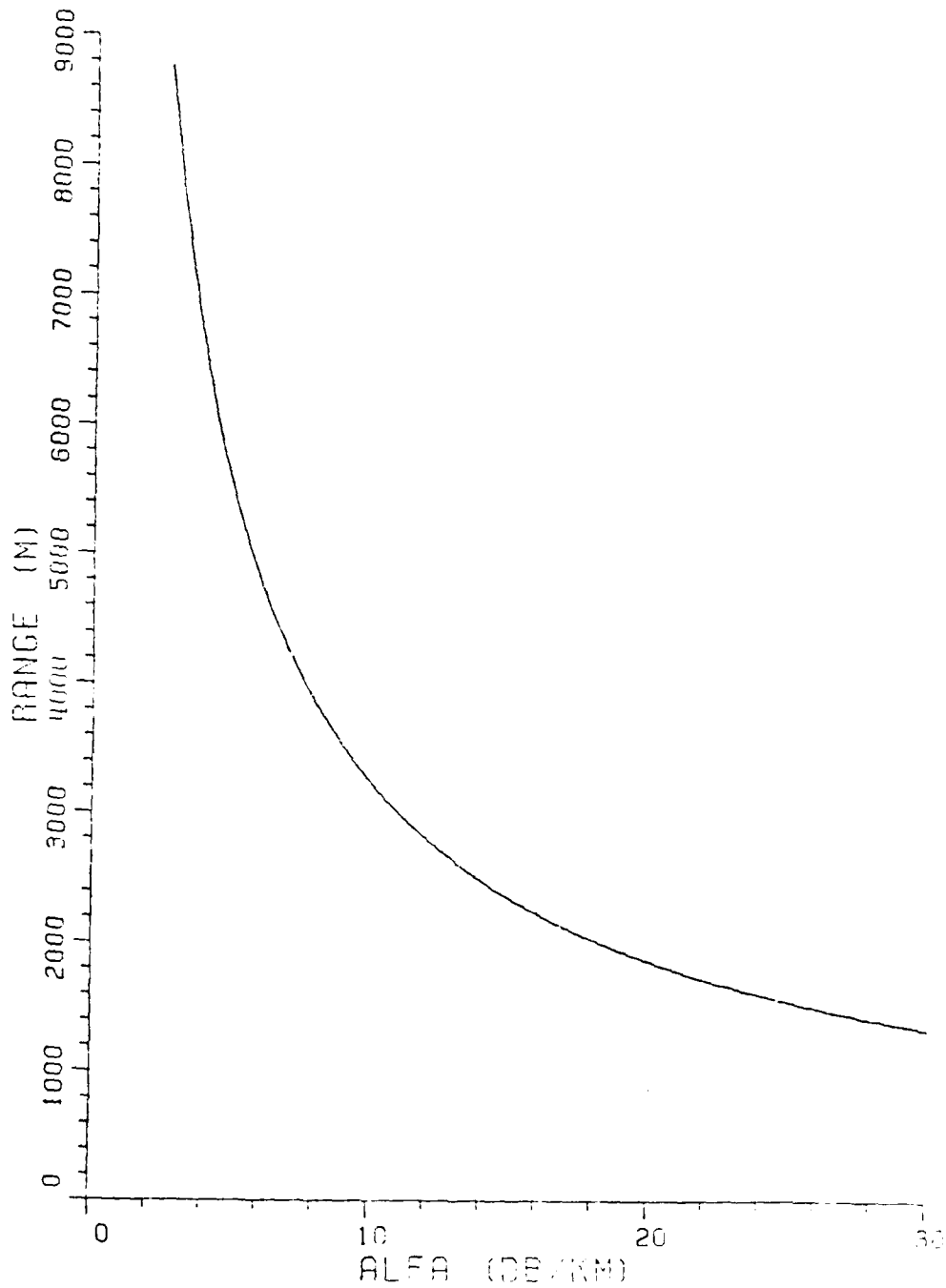


Figure 23. Range versus specific attenuation for $E/N=10$ dB for the radar system with post-detection integration. Power transmitted $P_t=1$ Kw, intermediate frequency bandwidth $B_{if}=10$ MHz, number of pulses $n=100000$.

The equations used to develop this program are Equation (57) in Chapter II, and Equations (A59), (A63) and (A64) in Appendix A. The calculated extinction due to rain is shown in Figure 24.

This subroutine was applied to plot maximum attainable range for the system with the quadrature receiver. The results are shown in Figure 25. The routine can be used equally well with the other systems discussed in Section II.

The rain drop size distribution is supplied as a subprogram. By changing this subprogram, the same routine may be used to calculate extinction due to rain with other expressions or empirical data for size distribution. This is useful because the distribution of the smaller drops becomes important in the millimeter-wave range, and the distributions given in the literature differ most for small drop sizes. Given the appropriate size distribution, the routine can handle attenuation through fog as well.

D. Conclusions

Five systems considered for transmission measurements at 94 GHz were studied. One of these systems measures transmission directly from the transmitter to the receiver. The other four systems are single-ended, i.e., they operate like a radar measuring signals that are reflected from a calibrated target. Each single-ended system employs a different signal processing scheme.

It was found that much better range values can be acquired with the two-ended system especially under severe weather conditions. This is mainly because with this system, the path over which the signal suffers an exponential decay is only half of what it is with the other systems. The single-ended systems however have the advantage of the ease with which range can be varied. This involves transporting only the target. If for this reason one wishes to use a single-ended system,

it was found that the best performance is achieved with a quadrature receiver. This is due to the linear nature of this receiver which becomes important especially for low values of signal-to-noise ratio at the input of the detector.

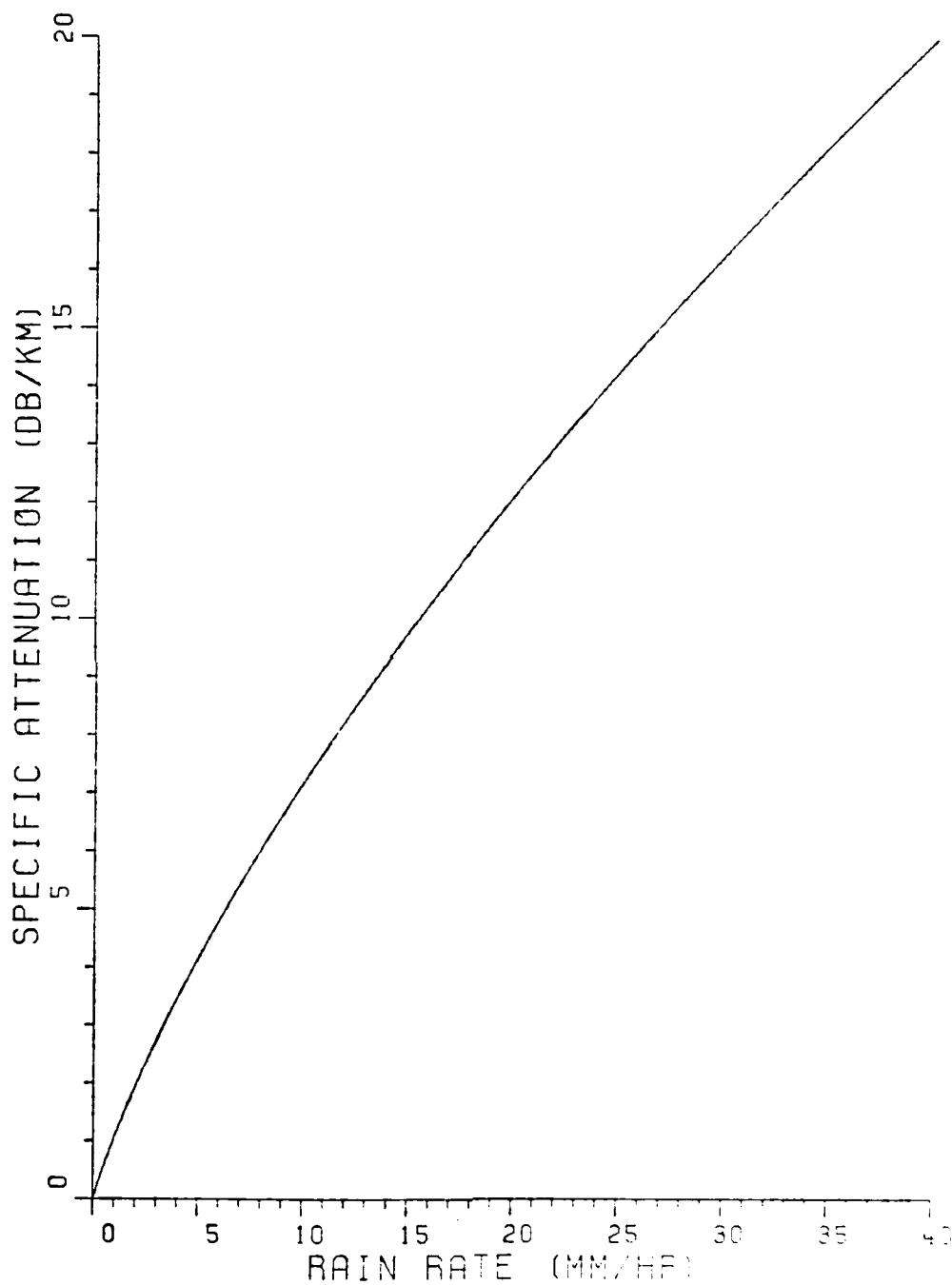


Figure 24. Specific attenuation versus rain rate at 94 GHz with Marshall and Palmer drop size distribution.

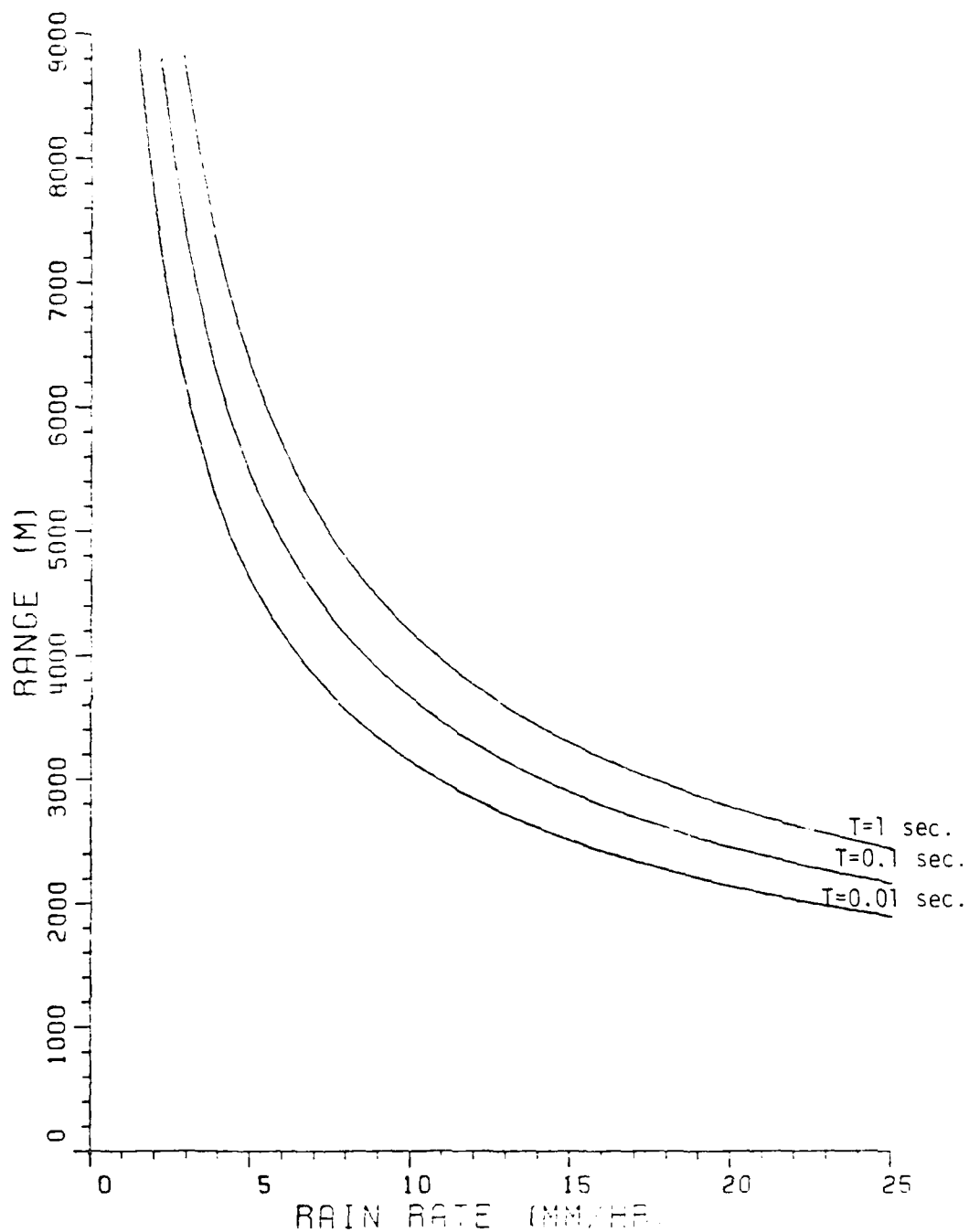


Figure 25. Range versus rain rate for $E/N=10$ dB for the single-ended system with quadrature receiver. T : integration time.

APPENDIX A SCATTERING FROM A SPHERE

The problem of scattering from a sphere was first solved by Mie[7]. The solution has been reproduced in various textbooks; the treatment given here follows Kerker[8] and was undertaken primarily to check the formulas used for computation. It differs from Kerker's derivation in that, instead of the traditional Hertz potentials, the currently more popular vector potential formulation is used.

In a homogeneous, source-free region, Maxwell's Equations for $e^{j\omega t}$ time dependence are given by

$$\nabla \times \bar{E} = j\omega \mu \bar{H} \quad , \quad (A1)$$

$$\nabla \times \bar{H} = j\omega \epsilon \bar{E} \quad , \quad (A2)$$

$$\nabla \cdot \bar{H} = 0 \quad , \quad (A3)$$

$$\nabla \cdot \bar{E} = 0 \quad , \quad (A4)$$

where μ , ϵ are constants, which may be complex. Equations (A3) and (A4) suggest that the fields can be expressed in terms of a magnetic vector potential \bar{A} and a dual electric vector potential \bar{F} . \bar{A} and \bar{F} satisfy the equations[12]

$$\nabla \times \nabla \times \bar{A} - k^2 \bar{A} = -j\omega \mu \nabla^2 \bar{A} \quad , \quad (A5)$$

and

$$\nabla \times \nabla \times \bar{F} - k^2 \bar{F} = -j\omega\epsilon \bar{f} \quad , \quad (A6)$$

where a and f are arbitrary scalars. The field quantities in terms of the vector potentials are given by

$$\bar{E} = -\nabla \times \bar{F} + \frac{1}{j\omega\epsilon} \nabla \times \nabla \times \bar{A} \quad , \quad (A7)$$

and

$$\bar{H} = \nabla \times \bar{A} + \frac{1}{j\omega\mu} \nabla \times \nabla \times \bar{F} \quad . \quad (A8)$$

Let

$$\bar{A} = \hat{r} A_r \quad , \quad (A9)$$

and

$$\bar{F} = \hat{r} F_r \quad , \quad (A10)$$

so that the fields can be expressed as a superposition of two parts, one TM to r and one TE to r , where \hat{r} is the outward directed unit vector. A convenient way to completely define the vector potentials is to let

$$-j\omega\epsilon a = \frac{\partial A_r}{\partial r} \quad , \quad (A11)$$

and

$$-j\omega\mu f = \frac{\partial F_r}{\partial r} \quad . \quad (A12)$$

Then, from Equations (A5) and (A6), one obtains

$$\frac{\partial^2 P_r}{\partial r^2} + \frac{1}{r^2 \sin \theta} \frac{\partial}{\partial \theta} \left(\sin \theta \frac{\partial P_r}{\partial \theta} \right) + \frac{1}{r^2 \sin^2 \theta} \frac{\partial^2 P_r}{\partial \phi^2} + k^2 P_r = 0 \quad (A13)$$

satisfied by both $P_r = A_r$ and $P_r = F_r$. Note that Equation (A13) is equivalent to

$$(\nabla^2 + k^2) \frac{A_r}{r} = 0 \quad , \quad (A14)$$

and

$$(\nabla^2 + k^2) \frac{F_r}{r} = 0 \quad . \quad (A15)$$

Define

$$\psi^a = \frac{A_r}{r} \quad , \quad (A16)$$

and

$$\psi^f = \frac{F_r}{r} \quad . \quad (A17)$$

Then, both of the ψ functions can be shown by use of Equation (A13) to satisfy

$$\frac{1}{r} \left(\frac{\partial^2 r \psi}{\partial r^2} \right) + \frac{1}{r^2 \sin \theta} \frac{\partial}{\partial \theta} \left(\sin \theta \frac{\partial \psi}{\partial \theta} \right) + \frac{1}{r^2 \sin^2 \theta} \frac{\partial^2 \psi}{\partial \phi^2} + k^2 \psi = 0 \quad , \quad (A18)$$

where $\psi = \psi^a$ or $\psi = \psi^f$. The field quantities in terms of these potentials are given by [12]

$$E_r = \frac{1}{j\omega \epsilon} \left(\frac{\partial^2}{\partial r^2} + k^2 \right) (r \psi^a) \quad , \quad (A19)$$

$$E_\theta = \frac{-1}{r \sin \theta} \frac{\partial (r \psi^f)}{\partial \phi} + \frac{1}{j\omega \epsilon r} \frac{\partial^2 (r \psi^a)}{\partial r \partial \theta} \quad , \quad (A20)$$

$$E_z = \frac{1}{r} \frac{\partial(r u^f)}{\partial r} + \frac{1}{j \omega r \sin \theta} \frac{\partial^2(r u^a)}{\partial r \partial \theta} \quad , \quad (A21)$$

$$H_r = \frac{1}{j \omega \mu} \left(\frac{\partial^2}{\partial r^2} + k^2 \right) (r u^f) \quad , \quad (A22)$$

$$H_\theta = \frac{1}{r \sin \theta} \frac{\partial(r u^a)}{\partial \theta} + \frac{1}{j \omega \mu r} \frac{\partial^2(r u^f)}{\partial r \partial \theta} \quad , \quad (A23)$$

and

$$H_\phi = -\frac{1}{r} \frac{\partial(r u^a)}{\partial \theta} + \frac{1}{j \omega \mu r \sin \theta} \frac{\partial^2(r u^f)}{\partial r \partial \theta} \quad . \quad (A24)$$

to solve Equation (A18), let

$$u(r, \theta, \phi) = R(r) \Theta(\theta) \Phi(\phi) \quad . \quad (A25)$$

This yields three ordinary differential equations given by

$$\frac{d^2[rR(r)]}{dr^2} + \left[k^2 - \frac{n(n+1)}{r^2} \right] rR(r) = 0 \quad , \quad (A26)$$

$$\frac{1}{\sin \theta} \frac{d}{d\theta} \left[\sin \theta \frac{d\Theta(\theta)}{d\theta} \right] + \left[n(n+1) - \frac{m^2}{\sin^2 \theta} \right] \Theta(\theta) = 0 \quad , \quad (A27)$$

and

$$\frac{d^2\Phi(\phi)}{d\phi^2} + m^2\Phi(\phi) = 0 \quad , \quad (A28)$$

where n is integer and non-negative, and m can assume the values $-n, -n+1, \dots, 0, 1, \dots, n-1, n$. Equation (A26) has the two independent solutions known as the Ricatti-Bessel Functions which are given by

$$\hat{j}_n(kr) = \sqrt{\frac{\pi kr}{2}} J_{n+1/2}(kr) \quad , \quad (A29)$$

and

$$N_n(kr) = \sqrt{\frac{\pi kr}{2}} N_{n+1/2}(kr) \quad . \quad (A30)$$

where $J_{n+1/2}$ and $N_{n+1/2}$ are half-integer order Bessel and Neumann Functions, respectively. The solutions to Equation (A27) are the Associated Legendre Polynomials given by

$$\Theta(\theta) = P_n^m(\cos\theta) \quad . \quad (A31)$$

For the solutions to Equation (A28), one obtains

$$\Phi(\phi) = \sin(m\phi), \quad \cos(m\phi) \quad . \quad (A32)$$

Supposing that an incident plane wave propagating along the z-axis has associated with it the electric field given by

$$\vec{E}^i = \hat{x} e^{-jk_0 z} \quad , \quad (A33)$$

then, for the scalar potentials, one obtains

$$r_\psi^{ia} = \frac{1}{k_0^2} \sum_{n=1}^{\infty} j^{(n-1)} \frac{2n+1}{n(n+1)} \hat{J}_n(k_0 r) P_n^1(\cos\theta) \cos\phi \quad , \quad (A34)$$

and

$$r_\psi^{if} = \frac{1}{k_0^2} \sum_{n=1}^{\infty} j^{(n-1)} \frac{2n+1}{n(n+1)} \hat{J}_n(k_0 r) P_n^1(\cos\theta) \sin\phi \quad . \quad (A35)$$

The scalar potentials for the scattered fields can be expressed as a similar series

$$r_\psi^{sa} = - \frac{1}{k_0^2} \sum_{n=1}^{\infty} j^{(n-1)} \frac{2n+1}{n(n+1)} a_n \hat{H}_n^{(2)}(k_0 r) P_n^1(\cos\theta) \cos\phi \quad , \quad (A36)$$

$$r_{\psi}^{sf} = - \frac{1}{k_0^2} \sum_{n=1}^{\infty} j^{(n-1)} \frac{2n+1}{n(n+1)} b_n \hat{H}_n^{(2)}(k_0 r) P_n^1(\cos\theta) \sin\phi, \quad (A37)$$

while potentials corresponding to the fields transmitted into the sphere are given by

$$r_{\psi}^{ta} = \frac{1}{k_1^2} \sum_{n=1}^{\infty} j^{(n-1)} \frac{2n+1}{n(n+1)} c_n \hat{J}_n(k_1 r) P_n^1(\cos\theta) \cos\phi, \quad (A38)$$

$$r_{\psi}^{tf} = \frac{1}{k_1^2} \sum_{n=1}^{\infty} j^{(n-1)} \frac{2n+1}{n(n+1)} d_n \hat{J}_n(k_1 r) P_n^1(\cos\theta) \sin\phi, \quad (A39)$$

where k_0 and k_1 are the wave numbers in air and in the sphere, respectively. The Ricatti-Hankel function is defined by

$$\hat{H}_n^{(2)}(kr) = \hat{J}_n(kr) - j\hat{N}_n(kr) = \sqrt{\frac{\pi kr}{2}} H_{n+1/2}^{(2)}(kr), \quad (A40)$$

where $H_{n+1/2}^{(2)}$ are the half-integer order Hankel Functions of the second kind. For ψ_r , only $\hat{J}_n(k_1 r)$ have been chosen, because $\hat{N}_n(k_1 r)$ are not finite at $r=0$. For ψ^s , functions which satisfy the radiation condition as r approaches infinity are needed and therefore $\hat{H}_n^{(2)}(k_0 r)$ have been used. The coefficients a_n , b_n , c_n and d_n can be found using the boundary conditions at $r=a$, the surface of the sphere, together with which Equations (A19) through (A24) yield

$$\frac{\partial}{\partial r} [r(\psi^{ia} + \psi^{sa})] = \frac{\partial}{\partial r} [r\psi^{ta}] \quad , \quad (A41)$$

$$\frac{\partial}{\partial r} [r(\psi^{if} + \psi^{sf})] = \frac{\partial}{\partial r} [r\psi^{tf}] \quad , \quad (A42)$$

$$j\omega\epsilon_0 r(\psi^{ia} + \psi^{sa}) = j\omega\epsilon_1 r\psi^{ta} \quad , \quad (A43)$$

$$j\omega\mu_0 r(\psi^{if} + \psi^{sf}) = j\omega\mu_1 r\psi^{tf} \quad . \quad (A44)$$

Since each term in the expansions is linearly independent from all the others, the boundary conditions may be matched for each value of n separately. Thus, for the first two coefficients, one obtains

$$a_n = \frac{\hat{J}_n(k_0 a) \hat{J}'_n(k_1 a) - n_c \hat{J}_n(k_1 a) \hat{J}'_n(k_0 a)}{\hat{H}_n^{(2)}(k_0 a) \hat{J}'_n(k_1 a) - n_c \hat{J}_n(k_1 a) \hat{H}_n^{(2)'}(k_0 a)}, \quad (A45)$$

and

$$b_n = \frac{n_c \hat{J}_n(k_0 a) \hat{J}'_n(k_1 a) - \hat{J}_n(k_1 a) \hat{J}'_n(k_0 a)}{n_c \hat{H}_n^{(2)}(k_0 a) \hat{J}'_n(k_1 a) - \hat{J}_n(k_1 a) \hat{H}_n^{(2)'}(k_0 a)}, \quad (A46)$$

where

$$\hat{J}'_n(x) = \frac{d}{dx} \hat{J}_n(x) \quad (A47)$$

and n_c is the relative refractive index at the sphere with respect to the external medium.

In the far zone of the sphere, the wave has only transverse components of the fields. Also, employing the limits

$$\lim_{x \rightarrow \infty} \hat{H}_n^{(2)}(x) = j^{(n+1)} e^{-jx} \quad (A48)$$

and

$$\lim_{x \rightarrow \infty} \hat{H}_n^{(2)'}(x) = j^n e^{-jx} \quad (A49)$$

the far zone fields become

$$E_\phi = \frac{-j e^{-jk_0 r}}{k_0 r} \sin \phi \sum_{n=1}^{\infty} \frac{2n+1}{n(n+1)} \left[a_n \frac{P_n^1(\cos \theta)}{\sin \theta} + b_n \frac{dP_n^1(\cos \theta)}{d\theta} \right], \quad (A50)$$

$$E_\theta = \frac{j e^{-jk_0 r}}{k_0 r} \cos \phi \sum_{n=1}^{\infty} \frac{2n+1}{n(n+1)} \left[a_n \frac{dP_n^1(\cos \theta)}{d\theta} + b_n \frac{P_n^1(\cos \theta)}{\sin \theta} \right], \quad (A51)$$

and

$$\vec{H} = \frac{\hat{k} \times \vec{E}}{Z_c}, \quad (A52)$$

where \hat{k} is the unit vector in the direction of propagation and Z_c is the free-space impedance given by

$$Z_c = \sqrt{\frac{\mu_0}{\epsilon_0}}. \quad (A53)$$

Define the scattering cross-section of the sphere as

$$C_{SCA} = \frac{\text{Re} \int (\vec{E}^S \times \vec{H}^{S*}) \cdot \hat{n} \, ds}{|\text{Re} \{ \vec{E}^i \times \vec{H}^i \}|} = Z_c \text{Re} \int (\vec{E}^S \times \vec{H}^{S*}) \cdot \hat{n} \, ds. \quad (A54)$$

In arriving at the last equality, the specific incident field of Equation (A33) was employed, \vec{E}_s , \vec{H}_s are the scattered fields corresponding to this incident field. Since, in general, the refractive index of the sphere, n_c , may be complex, some energy will be dissipated. Thus, define the extinction cross-section

$$C_{EXT} = C_{SCA} + C_{ABS}, \quad (A55)$$

where C_{ABS} is the absorption cross-section of the sphere. Consider the integral

$$\begin{aligned} & Z_c \text{Re} \oint [(\vec{E}^i + \vec{E}^S) \times (\vec{H}^i + \vec{H}^S)^*] \cdot \hat{n} \, ds \\ &= Z_c \text{Re} \int_0^\pi \int_0^{2\pi} (E_\theta^i H_\phi^{i*} - E_\phi^i H_\theta^{i*}) r^2 \sin \theta \, d\theta \, d\phi \\ &+ Z_c \text{Re} \int_0^\pi \int_0^{2\pi} (E_\theta^S H_\phi^{S*} + E_\phi^S H_\theta^{S*} - E_\theta^S H_\phi^{i*} - E_\phi^i H_\theta^{S*}) r^2 \sin \theta \, d\theta \, d\phi \\ &+ Z_c \text{Re} \int_0^\pi \int_0^{2\pi} (E_\theta^S H_\phi^{S*} - E_\phi^S H_\theta^{S*}) r^2 \sin \theta \, d\theta \, d\phi. \end{aligned} \quad (A56)$$

Considering that the surface on which the integrals are being evaluated does not enclose any sources, the first integral on the right-hand side which stands for the net outflux of energy in the unperturbed incident wave must be equal to zero. The third term obviously is C_{SCA} . If energy is to be conserved, the sum of the three terms must be equal to $-C_{ABS}$, since the sphere, absorbing energy, is the only energy sink. Therefore, the second term must equal $-C_{EXT}$. This integral has been evaluated and yields [7]

$$C_{EXT} = \frac{\lambda^2}{2\pi} \sum_{n=1}^{\infty} (2n+1) [\text{Re}(a_n + b_n)] \quad (A57)$$

The corresponding efficiency factor for extinction (dimensionless) is defined as

$$Q_{EXT} = \frac{C_{EXT}}{\pi a^2} \quad (A58)$$

From Equations (A57) and (A58), one obtains

$$Q_{EXT} = \frac{2}{(k_0 a)^2} \sum_{n=1}^{\infty} (2n+1) [\text{Re}(a_n + b_n)] \quad (A59)$$

The coefficients a_n and b_n may be expressed in terms of the Spherical Bessel and Hankel Functions using

$$\hat{J}_n(z) = \sqrt{\frac{\pi z}{2}} J_{n+1/2}(z) = z j_n(z) \quad , \quad (A60)$$

and

$$\hat{H}_n^{(2)}(z) = \sqrt{\frac{\pi z}{2}} H_{n+1/2}^{(2)}(z) = z h_n^{(2)}(z) \quad . \quad (A61)$$

The derivatives in the expressions for a_n and b_n can also be eliminated by use of the relationship given by [9]

$$\frac{d}{dz} g_n(z) = \frac{1}{2n+1} [n g_{n-1}(z) - (n+1) g_{n+1}(z)] \quad , \quad (A62)$$

where $g_n(z) = j_n(z)$ or $h_n^{(2)}(z)$.

Using these Equations. (A45) and (A46) become,

$$a_n = \frac{\left\{ j_n(k_0 a) \left[j_n(k_1 a) + \frac{n}{2n+1} k_1 a j_{n-1}(k_1 a) - \frac{n+1}{2n+1} k_1 a j_{n+1}(k_1 a) \right] \right.}{\left. \left[h_n^{(2)}(k_0 a) \left[j_n(k_1 a) + \frac{n}{2n+1} k_1 a j_{n-1}(k_1 a) - \frac{n+1}{2n+1} k_1 a j_{n+1}(k_1 a) \right] \right] \right\}} \cdot \frac{-n_c^2 j_n(k_1 a) \left[j_n(k_0 a) + \frac{n}{2n+1} k_0 a j_{n-1}(k_0 a) - \frac{n+1}{2n+1} k_0 a j_{n+1}(k_0 a) \right]}{\left\{ h_n^{(2)}(k_0 a) \left[j_n(k_1 a) + \frac{n}{2n+1} k_1 a j_{n-1}(k_1 a) - \frac{n+1}{2n+1} k_1 a j_{n+1}(k_1 a) \right] \right\}} \cdot \frac{-n_c^2 j_n(k_1 a) \left[h_n^{(2)}(k_0 a) + \frac{n}{2n+1} k_0 a h_{n-1}^{(2)}(k_0 a) - \frac{n+1}{2n+1} k_0 a h_{n+1}^{(2)}(k_0 a) \right]}{\left\{ h_n^{(2)}(k_0 a) \left[j_n(k_1 a) + \frac{n}{2n+1} k_1 a j_{n-1}(k_1 a) - \frac{n+1}{2n+1} k_1 a j_{n+1}(k_1 a) \right] \right\}} \quad (A63)$$

and

$$b_n = \frac{\left\{ j_n(k_0 a) \left[j_n(k_1 a) + \frac{n}{2n+1} k_1 a j_{n-1}(k_1 a) - \frac{n+1}{2n+1} k_1 a j_{n+1}(k_1 a) \right] \right.}{\left. \left[h_n^{(2)}(k_0 a) \left[j_n(k_1 a) + \frac{n}{2n+1} k_1 a j_{n-1}(k_1 a) - \frac{n+1}{2n+1} k_1 a j_{n+1}(k_1 a) \right] \right] \right\}} \cdot \frac{-j_n(k_1 a) \left[j_n(k_0 a) + \frac{n}{2n+1} k_0 a j_{n-1}(k_0 a) - \frac{n+1}{2n+1} k_0 a j_{n+1}(k_0 a) \right]}{\left\{ h_n^{(2)}(k_0 a) \left[j_n(k_1 a) + \frac{n}{2n+1} k_1 a j_{n-1}(k_1 a) - \frac{n+1}{2n+1} k_1 a j_{n+1}(k_1 a) \right] \right\}} \cdot \frac{-j_n(k_1 a) \left[h_n^{(2)}(k_0 a) + \frac{n}{2n+1} k_0 a h_{n-1}^{(2)}(k_0 a) - \frac{n+1}{2n+1} k_0 a h_{n+1}^{(2)}(k_0 a) \right]}{\left\{ h_n^{(2)}(k_0 a) \left[j_n(k_1 a) + \frac{n}{2n+1} k_1 a j_{n-1}(k_1 a) - \frac{n+1}{2n+1} k_1 a j_{n+1}(k_1 a) \right] \right\}} \quad (A64)$$

APPENDIX B

GENERATION OF THE SPHERICAL WAVE FUNCTIONS

Since the expressions for Mie coefficients a_n and b_n involve Spherical Bessel and Neumann Functions, the task of generating these functions in a fast and accurate manner was encountered. The aim has been to develop a scheme which could be used to evaluate the functions for very small arguments (of order 10^{-3}) so as to enable the use of the routine for the problem of modeling attenuation through fog. It has been found that for arguments as small as those of interest here, the direct recursion relationship satisfied by the Bessel Functions cannot be used since errors tend to propagate and significant digits are lost after only a few recursions.

Since Spherical Bessel Functions of integer order and Cylindrical Bessel Functions of half-integer order are related through

$$j_n(x) = \sqrt{\frac{\pi}{2x}} J_{n+1/2}(x) \quad , \quad (B1)$$

an equivalent problem is to generate half-integer order Bessel Functions. For this, depending on the magnitude of the real part of the argument, two methods were used.

1. Small $\text{Re}(x)$

The method employed here makes use of an auxiliary function which is closely related to the Bessel Function [13]

$$\Lambda_\nu(x) = \frac{\Gamma(\nu+1)}{(x/2)^\nu} J_\nu(x) \quad , \quad (B2)$$

where Γ is the Gamma Function defined for real y by

$$\Gamma(y) = \int_0^{\infty} t^{y-1} e^{-t} dt \quad \text{for } y > 0, \quad (B3)$$

and $\Gamma(y)$ for $y < 0$ may be found using

$$\Gamma(y) = \frac{\Gamma(y+1)}{y}. \quad (B4)$$

Since the Bessel Functions satisfy the well-known recursion relationship

$$J_{\nu+1}(x) + J_{\nu-1}(x) = \frac{2\nu}{x} J_{\nu}(x), \quad (B5)$$

it can readily be shown that the auxiliary functions will satisfy

$$\Lambda_{\nu}(x) = \Lambda_{\nu-1}(x) + \frac{x^2}{4\nu(\nu+1)} \Lambda_{\nu+1}(x). \quad (B6)$$

It can also be shown by substituting into Equation (B2) that since

$$J_{\nu}(x) = \sum_{k=0}^{\infty} \frac{(-1)^k (x/2)^{\nu+2k}}{k! \Gamma(\nu+k+1)}, \quad (B7)$$

then, the Λ functions have the representation

$$\Lambda_{\nu}(x) = \sum_{k=0}^{\infty} \frac{(-1)^k (x/2)^{2k} \Gamma(\nu+1)}{k! \Gamma(\nu+k+1)}. \quad (B8)$$

The power series in Equation (B8) has been found to converge very fast for small arguments. First, the functions $\Lambda_{\nu}(x)$ for $\nu=61/2$ and $\nu=59/2$ were evaluated employing this power series expansion. In the process, only four terms of the series were considered. The GMMMA subroutine in the IBM Scientific Subroutine Package was used to evaluate the Gamma Functions. Then, using the recursion formula in Equation (B6) downward, $\Lambda_{\nu}(x)$ for positive, half-integer ν less than $59/2$ were obtained. Finally, the Spherical Bessel Functions were evaluated by use of

Equations (B1) and (B2). This method was used for arguments which satisfy

$$\text{Re}(x) \leq 3.4 .$$

2. Large Re(x)

The recursion relationship satisfied by the Spherical Bessel Functions

$$j_{n+1}(x) = \frac{2n-1}{x} j_n(x) - j_{n-1}(x) , \quad (\text{B9})$$

and the two identities

$$j_0(x) = \frac{\sin x}{x} , \quad (\text{B10})$$

and

$$j_1(x) = \frac{j_0(x) - \cos x}{x} \quad (\text{B11})$$

were used to evaluate $j_n(x)$ for $n \leq n_c$, where n_c is the largest integer smaller than or equal to $\text{Re}(x)$. Then, starting with an arbitrary value of $j_{29}(x)$ and 0 for $j_{30}(x)$, the recursion formula in Equation (B9) was used to find $j_n(x)$ for $n \geq n_c$. Finally, the preliminary values of $j_n(x)$ for $n_c < n \leq 30$ were scaled by the same constant so as to match the value of $j_{n_c}(x)$ found by forward recursion. This method was used for the arguments which satisfy $\text{Re}(x) > 3.4$.

To generate the Spherical Neumann Functions, Bessel Functions $J_\nu(x)$ for half-integer $\nu \leq -3/2$ were calculated using Equation (B5) and the two values given by

$$J_{1/2}(x) = \sqrt{\frac{2x}{\pi}} \frac{\sin x}{x} , \quad (\text{B12})$$

and

$$J_{-1/2}(x) = -\sqrt{\frac{2x}{\pi}} \frac{\cos x}{x} \quad (B13)$$

Then, the Spherical Neumann Functions were evaluated using

$$n_\nu(x) = (-1)^{\nu+1} \sqrt{\frac{\pi}{2x}} J_{-(\nu+1/2)}(x) \quad (B14)$$

Both the Spherical Bessel and Neumann Functions thus generated using single precision were checked against "Tables of Spherical Bessel Functions"[13] and were found to be accurate to five significant digits.

REFERENCES

1. Rosenblum, E.S., "Atmospheric Absorption of 10 to 400 KCPS Radiation," Microwave Journal, (March 1961), pp. 91-96.
2. Skolnik, M.I., Introduction to Radar Systems, McGraw-Hill, 1962.
3. Middleton, D., Statistical Communication Theory, McGraw-Hill, 1960.
4. Schwartz, M., Information Transmission, Modulation, and Noise, McGraw-Hill, 1970.
5. Haykin, S., Communication Systems, John Wiley and Sons, 1978.
6. Marcum, J.I., "A Statistical Theory of Target Detection by Pulsed Radar, Mathematical Appendix," IRE Trans. on Information Transmission, Vol. 6, (1945), pp. 46-156.
7. Mie, G., "Considerations on the Optics of Turbid Media, Especially Colloidal Metal Sols," Annalen der Physik, Vol. 25, (1908), p. 377.
8. Kerker, M., Scattering of Light, Academic Press, 1969.
9. Stratton, J.A., Electromagnetic Theory, McGraw-Hill, 1941.
10. Marshall, J.S. and Palmer, W.M.K., "The Distribution of Rain-drops with Size," J. Meteor., Vol. 5, (1948), pp. 165-166.
11. Davies, M., Pardoe, G.W.F., Chamberlain, J. and Gebbie, H.A., "Submillimetre- and Millimetre-Wave Absorptions of Some Polar and Non-Polar Liquids Measured by Fourier Transform Spectroscopy," Faraday Society Transactions. Vol. 66, (1970), pp. 273-292.
12. Harrington, R.F., Time Harmonic Electromagnetic Fields, McGraw-Hill, 1961.
13. Mathematical Tables Project, National Bureau of Standards, Tables of Spherical Bessel Functions, Columbia University Press, 1947.

AFWAL-TR-81-1281
Distribution List

<u>Organization</u>	<u>No. of Copies</u>
AFWAL/AARI-1 Attn: R. Rang Wright-Patterson AFB, OH 45433	5
DTIC Cameron Station Alexandria, VA 22314	12
HQ USAF/SAMID Washington, DC 20330	1
AFSC/IN Andrews AFB, MD 20334	1
AUL/LSE Maxwell AFB, AL 36112	1
AFWAL/TST-2 Wright-Patterson AFB, OH 45433	1
AFELC/ESRI San Antonio, TX 78243	3
USA Night Vision and Electro-Optical Laboratories Attn: DELNV-AC (R. Wright) Ft Belvoir, VA 22060	1
Commander USA - Atmospheric Science Lab Attn: DELAS-EO-EN (D. Snyder) WSMR, NM 88022	1
US Army Missile Command Attn: DRMSI-REL (Mr T. Barley) Redstone Arsenal, AL 35898	1
Naval Weapons Center Attn: Mr D. Dobberpuhl (Code 31506) China Lake, CA 93555	1
AFGL/LYR Attn: Maj Mike Snapp Hanscom AFB, MA 01731	1
AFGL/OPI Hanscom AFB, MA 01731	1
AFWAL/TST-1 WPAFB OH 45433	1

<u>Organization</u>	<u>No. of Copies</u>
AFWAL/WEA Wright-Patterson AFB, OH 45433	1
EOARD Attn: Lt Col Peter Soliz Box 14 FPO New York, NY 09510	1
AFGL/LYS Attn: Vince Falcone Hanscom AFB, MA 01731	1
AFGL/OPI Attn: Lt Col Kit Cottrell Hanscom AFB, MA 01731	1
AFGL/LYS Attn: Dr Mike Kraus Hanscom AFB, MA 01731	1
USAF ETAC/ONE Attn: Capt Michael Abel Scott AFB, IL 62225	1
HQ AWS/DOOE Attn: Lt Col Bob Wright Scott AFB, IL 62225	1
AFWAL/AAAS-2 Attn: Dianne Sommers Wright-Patterson AFB, OH 45433	1
AFWAL/AARI-3 Attn: Leo Vroombout Wright-Patterson AFB, OH 45433	1
AFWAL/AARI-3 Attn: Roger Cranos Wright-Patterson AFB, OH 45433	1
AFWAL/AARM-4 Attn: Walt Barnes Wright-Patterson AFB, OH 45433	1
AFWAL/AARM-4 Attn: Ralph Becker Wright-Patterson AFB, OH 45433	1
AFWAL/AART-2 Wright-Patterson AFB, OH 45433	1
AFWAL/AART-3 Attn: Clint Coombs Wright-Patterson AFB, OH 45433	1

<u>Organization</u>	<u>No. of Copies</u>
AFWAL/AART-3 Attn: Lt Mark Schulte Wright-Patterson AFB, OH 45433	1
AFWAL/AADM-2 Wright-Patterson AFB, OH 45433	1
AFWAL/AARF-4 Attn: L. Crouch Wright-Patterson AFB, OH 45433	1
ASD/ENAMD Wright-Patterson AFB, OH 45433	1
ASD/RWNM Attn: Mr Benitez Wright-Patterson AFB, OH 45433	1
AFWAL Liaison Office AD/XRG (AFWAL) Eglin AFB, FL 32542	2
Quest Research Corporation 4999 Northcutt Place Suite 2 Dayton, OH 45414	1
Science Applications, Inc. Attn: Mr Wasky 1010 Woodman Drive Suite 200 Dayton, OH 45432	1
Harry Diamond Laboratories Attn: Dr J. Namarich 2800 Powder Mill Road Adelphi, MD 20783	1
Ohio State University Electro Science Laboratory Attn: Dr C. Levis 1320 Kinnear Road Columbus, OH 43212	5
Alpha Industries, Inc. Attn: R. Gerrich 20 Sylvan Road Woburn, MA 01801	1

<u>Organization</u>	<u>No. of Copies</u>
U.S. Naval Weapons Center, Code 3313 Attn: Gaylon E. Ryno China Lake, CA 93555	1
The Aerospace Corporation Attn: Howard E. King Bldg. 120, Room 2011 2350 East El Segundo Blvd. El Segundo, CA 90245	1
Dept. of the Army Harry Diamond Laboratories 2800 Powder Mill Rd. Adelphi, MD 20738 Attn: A. Sindoris	1
USA CORADCOM CENCOMS DRDCO-COM-RH-1 Ft. Monmouth, N.J. 07703 Attn: Dr. Felix Schwerling	1
Office of Naval Research, Code 427 800 North Quincy St. Arlington, VA 22217 Attn: Dr. R. Collins	1
U.S. Army Research Office P.O. Box 12211 Research Triangle Park North Carolina 27709 Attn: Dr. W.A. Flood	1
U.S. Navy Naval Ocean Systems Center Attn: Dr. John Hoffman, Code 8255 San Diego, CA 92152	1
Jet Propulsion Laboratory Attn: Dr. E.K. Smith, MS 161-228 4800 Oak Grove Drive Pasadena, CA 91109	1
Lincoln Laboratory, MIT Attn: Dr. Alan Simmons Lexington, MA 02173	1

Organization

No. of Copies

Georgia Institute of Technology
Engineering Experiment Station
Attn: David Schmieder
Atlanta, GA 30332

1

Georgia Institute of Technology
Engineering Experiment Station
Attn: Dr Jim Echard
Atlanta, GA 30332

1

Georgia Institute of Technology
Engineering Experiment Station
Attn: Dr Robert McMillan
Atlanta, GA 30332

1

NASA Goddard Space Flight Center
Attn: Dr David Atlas, Code 910
Greenbelt, MD 20771

1

RADC/EEP
Attn: Dr Paul Kossey
Hanscom AFB, MA 01731

1

NASA Headquarters, EC-4
Attn: Dr Louis J. Ippolito
Washington, D.C. 20546

1

END

DATE
FILMED

4 - 83

DTIC